Nearshore Applications of Marine Radar

JD Lentine

15 June 2006

A project in fulfillment of the
Master's of Science in Civil Engineering,
Oregon State University

Table of Contents

List of Figures

List of Tables

1. Introduction

As the coastal communities of the United States grow there is an increasing need for new coastal infrastructure. Coastal engineering applications such as designing a breakwater or predicting the erosion along a beach require ocean wave properties such as wave period, wave direction and significant wave height. Additionally, there is an increasing need to better understand the sustainability of our coasts as we increase our infrastructure. Phenomena such as the rise in sea level and the shift in sediment transport due to coastal construction are constantly redefining our coastlines. These and other coastal phenomena occur on time scales of weeks to decades. Thus long term monitoring using a variety of coastal monitoring systems is needed to better understand coastal phenomena and assess the sustainability of the coasts.

The Northwest Association of Networked Ocean Observing Systems (NANOOS) is a regional association charged with the development and maintenance of an observing system for the Pacific Northwest. Under the auspices of the NANOOS-Pilot project a mobile autonomous radar remote sensing system is being developed at Oregon State University. The system, when completed, will be used as a wave monitoring system at the Mouth of the Columbia River (MCR). The information retrieved from the wave monitoring system will be tied into the NANOOS-Pilot program for research and distribution to the public. A "proof of concept" field deployment of the wave monitoring system was completed in January of 2006 at the MCR.

In Situ Point Measurements vs. Remote Sensing

In situ point sensors, such as buoys or bottom mounted pressure sensors are established ocean wave property retrieval systems. In situ point sensors provide excellent temporal resolution because of their high sampling rate capability. They are readily available and used by a variety of commercial, state and federal research agencies. However, in situ point sensors have to be deployed into and survive within the harsh ocean environment. Equipment and personnel are often damaged in rough sea deployments. They must withstand wave forces, ocean currents, marine growth, and salt water immersion. In situ point sensors must be constantly monitored and regularly maintained to ensure their successful operation.

Bottom mounted pressure sensors and buoys require minimum depths to operate properly, thus they are limited in their study of nearshore processes. In situ point sensors do not provide

adequate spatial resolution as they only cover a single point within the nearshore environment. Banks of in situ point sensors are possible, but are more expensive and require more maintenance.

Remote sensing is the logical choice for studying nearshore processes. Unlike point sensors, they allow researchers to obtain information over the entire nearshore area of study. Every digitized pixel in the remotely sensed area can be thought of as representing a "virtual" wave gauge. Methods of nearshore remote sensing include: Space-borne (satellite) radar, Synthetic Aperture Radar (SAR), High Frequency (HF) radar, Video and X-Band radar.

Space-borne radar and SAR remote sensing systems are limited by their ability to provide long term temporal information due to their lack of time on scene. Shore-based remote sensing systems, such as video and radar remote sensing systems, can be set up at coastal sites and offer much longer times on scene. The Coastal Imaging Lab (CIL) in the College of Oceanic and Atmospheric Sciences at Oregon State University has developed a suite of methods to analyze nearshore processes using video remote sensing. The CIL analyzes data from eleven shore based video remote sensing stations located at selected study sites around the globe. These stations are referred to as Argus stations. Shore based remote sensing systems avoid the problems associated with deployment and maintenance of in situ point sensors in the marine environment. Logistically there is minimal adjustment to the equipment for each individual deployment as the system is designed to function in a variety of environments. Deployment of shore based remote sensing systems can typically be made in harsh weather without worry of damage to equipment or personnel.

Video remote sensing systems are limited to daylight hours and can not be used during environmental conditions that affect visibility (storms, hurricanes, rain, fog, etc…). X-Band radar is generally less hampered by weather conditions and can be used in all light conditions. X-Band radar remote sensing systems provide spatial resolution on the order of 9 to 12 meters for ranges on the order of kilometers.

Radar is a mature technology that has been in use since the early part of the 20th century. The understanding and application of radar significantly advanced during the early part of World War II due to its military applications. Radar was designed to detect and calculate the range to a target using electromagnetic energy generated in short pulses. Radar is an acronym for "radio detecting and ranging."

Electromagnetic waves can be described by their amplitude, wavelength and frequency. Electromagnetic waves are composed of an electric and magnetic field. The magnetic field is oriented on the same axis as the electric field for vertically polarized (VV) electromagnetic waves and shifted 90 degrees for horizontally polarized (HH) electromagnetic waves.

A pulse modulated radar system tracks the time that it takes for a radiated pulse of electromagnetic energy to travel to and from the target. The distance to the target is calculated from the relationship of speed (c), range (R) and time (T). The time for the range calculation must be divided by two since the electromagnetic pulse travels to and from the target. Therefore the range is $R = \frac{T}{2 \times c}$. The speed of the radiated electromagnetic energy, c, is the speed of light. The free space velocity of light is 3.0 x 10^8 m/s. The azimuth of the target can also be recorded if the radar is equipped with a rotating antenna.

Figure 1 shows the basic the basics components of a pulse modulated radar system.

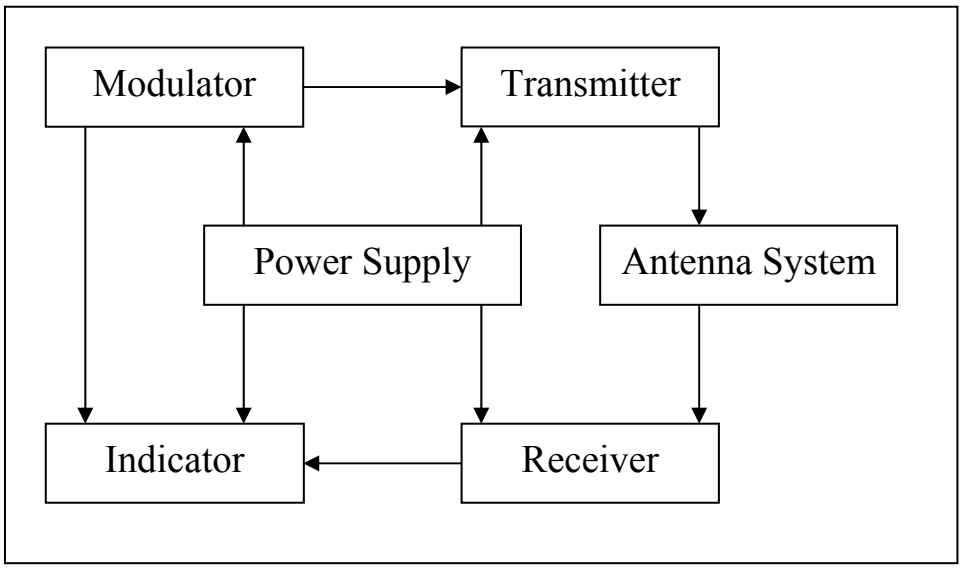

Figure 1 - The Basic Components of a Pulse Modulated Radar (DMA 1994).

The power supply provides the energy necessary for the operation of the radar system. The modulator synchronizes all the components of the radar system and ensures that the electromagnetic waves created by the transmitter are of the desired frequency. The transmitter generates the electromagnetic energy in the form of short pulses based on signals from the

modulator. The antenna focuses and transmits the electromagnetic energy generated by the transmitter. The antenna also receives the electromagnetic energy returned from a target. The receiver amplifies returned electromagnetic energy. The indicator produces a visual interpretation of returned electromagnetic energy.

Radar systems are classified by the wavelength of their emitted frequency. Marine radars are typically X or S-Band. Table 1 lists radar system classifications based on frequency and wavelength.

Band	Frequency	Wavelength
HF	3-30 MHz	10-100 m
VHF	30-300 MHz	1-10 m
UHF	300 MHz-1 GHz	30 cm-1 m
L-band	1-2 GHz	15-30 cm
S-band	2-4 GHz	7.5-15 cm
C-band	4-8 GHz	3.75-7.5 cm
X-band	8-12 GHz	2.5-3.75 cm
Ku-band	12-18 GHz	1.67-2.5 cm
K-band	18-27 GHz	1.11-1.67 cm
Ka-band	27-40 GHz	7.5 mm-1.11 cm
V-band	40-75 GHz	4-7.5 cm
W-band	75-110 GHz	2.7-4 mm
mm-band	110-300 GHz	1-2.7 mm

Table 1 - Radar classifications (Raemer 1997).

The pulse length of the radar determines the range resolution of the radar. The range resolution is the distance required by the radar to distinguish between two targets. The pulse length is the transmission time of a single pulse of electromagnetic energy. Pulse lengths for conventional radars are measured in microseconds (μsec) and nanoseconds (nsec) for high resolution radars.

The pulse length also determines the minimum distance that the radar can detect objects. For example if the pulse length is 1 μsec the minimum range an object can be detected is the same as the range resolution, 150 meters. The angular resolution is governed by the beam width of the

antenna. The pulse repetition frequency (PRF) is the number of pulses transmitted per second. The power of the radar system combined with the PRF determines the range of the radar system. Table 2 lists radar range resolutions based on pulse length.

Pulse Length	Best Attainable Range Resolution
.1 nsec	1.5 cm
1 nsec	15 cm
10 nsec	1.5 m
1 μsec	150 m
10 μsec	1500 m
100 μsec	15 km
100 msec	150 km

Table 2 - Best attainable range resolution based on pulse length (Raemer 1997).

Radar backscatter is produced from the interaction of electromagnetic waves and the rough surface of the ocean. The backscatter of the ocean surface is often called "Sea Clutter." Historical research of ocean backscatter was aimed at suppression of the phenomena. Yet, even after several decades of research, the mechanisms that produce backscatter from the ocean surface are not fully understood. One thing is for certain, though, the modulation of the sea clutter by gravity waves produces coherent wave modulation in the marine radar signal. Clear shipboard observations of these coherent wave modulations in the 1960s lead scientist to believe that marine radars could be used as an effective tool in measuring ocean wave properties.

Electromagnetic energy is backscattered from the ocean surface by two general methods. Specular reflection is mirror-like reflection that is most prevalent for small angles of incidence. The incidence angle is the angle that the incident ray makes with the normal to the surface. The grazing angle is complement of the incidence angle. In specular reflection the electromagnetic energy is reflected directly off the surface of the water. Bragg scattering is resonant reflection that occurs when electromagnetic energy interacts with waves that have a similar wavelength as the transmitted electromagnetic waves. Small scale capillary waves on the order of 1 to 3 cm provide the source for Bragg resonant scattering of marine X-band radars. Thus, the presence of wind is required to create these small scale waves in order for X-Band radars to image ocean waves. The intensity of the backscattered energy is most affected by the magnitude of the wind

velocity, the incidence angle of the emitted electromagnetic energy, and the azimuth angle of the radar relative to the crest of the wave. Bragg scattering is strongest when the radar azimuth angle is aligned with the wave direction.

Wright (1968) developed a composite surface model to predict the backscatter of the ocean surface. In the composite surface model Bragg waves ride on top of and are modulated by gravity waves. The composite surface theory satisfies backscatter returns for almost all angles of incidence. However, as the angle of incidence approaches 90 degrees (grazing incidence) the situation becomes more complicated and the composite theory does not accurately predict backscatter from the ocean surface. Phenomena, such as wave breaking and wave steepness, complicate the development of a model that accurately predicts backscatter of the ocean surface. The turbulence created by breaking waves presents areas of increased backscatter and steep waves present multiple paths of reflection that increase backscatter.

Tilt angle modulation, hydrodynamic modulation and shadowing modulate the ocean surface backscatter allowing the gravity waves to be imaged on the radar. Tilt modulation is a purely geometrical phenomenon that is created by gravity waves "tilting" the ocean surface towards and away from the radar. Radar backscatter increases as the wave is tilted towards the radar and decreases as the wave is tilted away from the radar. Tilt modulation is most prevalent when the radar beam is perpendicular to the wave front. Tilt modulation provides no contribution to the backscatter if the wave crest is parallel to the radar beam. Hydrodynamic modulation is caused by the change in shape of the small scale waves that cause Bragg scattering. Capillary waves increase in amplitude and decrease in wavelength on the front of gravity waves and decrease in amplitude and increase in wavelength on the back of gravity waves. The modulation of the small scale capillary waves on the front of the wave leads to a higher amount of backscatter on the front part of the wave. Shadowing occurs when the crest of one wave prevents illumination of the following trough. Thus a "shadow zone" is created between successive crests. Shadowing is the most prevalent modulating mechanism at high angles of incidence (Dankert et al 2004).

History of X-Band Remote Sensing

Radar remote sensing has continued despite the lack of a clear understanding of the mechanisms that produce and modulate ocean surface backscatter. Initial marine radar remote research was conducted on the plan position indicator (PPI) of shipboard radars in the 1960s. Researchers

measured wave direction and wavelengths directly on the radar screen. In the 1970s photographs were taken of the PPI that allowed researchers to manipulate the images and measure wave properties more accurately by hand.

X-Band radar research was significantly advanced in the 1980s when technology was developed that allowed researchers to digitally scan photographs taken from radar scopes. This allowed researchers to use computer FFT algorithms to calculate wave lengths and periods providing a more accurate estimation of ocean wave properties. Young and Rosenthal (1985) clearly described the methods to retrieve spectral information from x-band radars using successive photographs of radar images. Further developments in technology allowed researchers to start digitally recording data directly from the radar in the 1990s. For example, the signal to noise ratio of the radar return was used to calibrate marine radar remote sensing systems for the purpose of measuring significant wave height. Radar remote sensing technology can now be obtained commercially. The wave and surface current monitoring system, WAMOS, was developed at the German Research Center, GKSS, in 1995 and is commonly used today on offshore platforms. Recently, radar remote sensing research has focused on more accurately describing the physics of ocean wave backscatter and developing models that more correctly estimate wave properties from radar data. Also, engineering applications of radar remote sensing such as depth retrieval and surface current mapping are being tested.

The methodology developed for WAMOS at GKSS represents the standard in the analysis of ocean wave properties. WAMOS digitally records successive radar images to obtain wave field information in space and time. The mean intensity of the sea clutter is removed from the images to minimize the static spatial and temporal contributions to the spectrum. Sub areas of the image are then selected for analysis (Nieto Borge et al 2000).

The 3D spectrum of the image time series is estimated by the application of a 3D FFT algorithm. A highpass filter is then applied to remove low frequencies not associated with wind waves. Determination of the surface current is necessary to correct the doppler shift in the linear dispersion relationship. The surface current is estimated using a least squares method to fit the prevalent spectral energy to the dispersion shell created by the linear dispersion relationship. Periods and wavenumbers will be incorrectly associated if the surface current is not corrected for.

All energy from the 3D spectrum that does not lie on the dispersion shell is removed once the surface current has been calculated and the prevalent energy has been fitted to the dispersion shell. Then the image transfer function is applied to the 3D spectrum to connect the image spectrum to the wave spectrum. Finally, the signal to noise ratio (SNR) is used to calibrate the radar so that significant wave height can be estimated (Nieto Borge et al 2000). Calibration requires an in situ point sensor located within the area imaged by the radar to correlate SNR with wave height.

2. Field Deployment 1

2.1 Field Site

The U.S Army Corps of Engineers (USACE) *Field Research Facility* (FRF) is located in Duck, NC, on the Atlantic side of the North Carolina Outer Banks. The FRF is a branch of the USACE *Coastal and Hydraulics Laboratory* (CHL), which directs the coastal engineering research of the Corps of Engineers. The FRF was established in 1977 on the grounds of a 176 acre Navy bombing range that was available as surplus government property. The facility consists of a 560 meter long research pier, a main office building, two field support buildings, and an observation tower. The primary mission of the FRF is to collect measurements of meteorological and geomorphologic processes and understand the relations between them. The mission is accomplished by a small, highly skilled field staff, a multitude of in situ and remote sensors and several unique vehicles that support the monitoring program.

The FRF provides a dependable means of obtaining accurate and comprehensive measurements in all weather conditions. Wave height and period are available and published on their website from four different sensors, wave direction is immediately available from one sensor and standard meteorological information is available from two sensors. The sensors used in this study, and their station identifier, are the NOAA NDBC weather station (DUCN7), the beach bottom mounted pressure sensor (641), the end of the pier Baylor wave gauge (625), the eight meter pressure array (111, 161, 191, 211 and 251) and the directional Waverider buoy (630). The availability and high quality of FRF data make it ideal for testing remote sensing sensors and techniques.

In light of this, an X-Band radar experiment was conducted at the FRF, from September 26th to September 30th, 2005. Merrick C. Haller, an assistant professor in the Ocean Engineering division of the Civil, Construction and Environmental Engineering Department of Oregon State University, was the principal investigator. Video remote sensing data for comparison with collected radar data was collected from the FRF Argus station run by the Coastal Imaging laboratory in the College of Oceanic and Atmospheric Sciences at Oregon State University. The radar remote sensing system used for the experiment was purchased from Imaging Science Research, Inc, a small business in Virginia that specializes in radar remote sensing.

The pressure, wind speed and wind direction during the FRF experiment are shown in Figure 2.

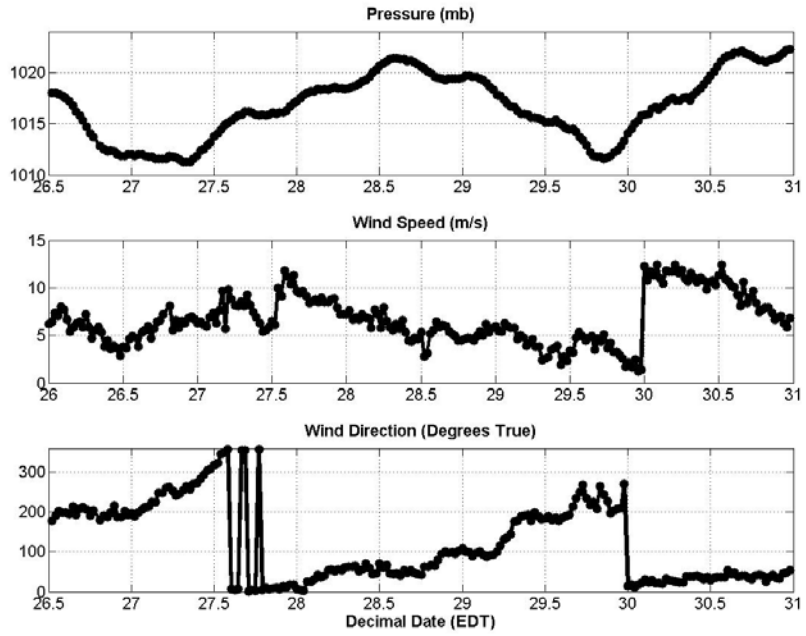

Figure 2 - Atmospheric pressure, wind speed and wind direction for the FRF field deployment.

There were two prominent drops in atmospheric pressure during the FRF experiment. The first drop in atmospheric pressure was very gradual. The lowest atmospheric pressure occurred at decimal date 27.19. The second drop in atmospheric pressure was much sharper than the first. The lowest atmospheric pressure for the second drop occurred at decimal date 29.73. Spikes in wind speed followed the drops in atmospheric pressure. The wind speed increased from 5.4 m/s at decimal date 27.27 to 11.8 m/s at decimal date 27.42. The wind speed spiked again from 1.2 m/s at decimal date 29.79 to 12.3 m/s at decimal date 29.83. The second spike in wind speed was more pronounced than the first. Increases in wind speed should produce a corresponding increase in backscatter from the ocean surface.

Shifts in the wind direction also followed the drops in atmospheric pressure. The wind shifted almost 160 degrees over the course of a day as the pressure dropped gradually at the beginning of the experiment. The next shift in the wind was much more pronounced than the first. The wind shifted from 271 degrees True at decimal date 29.81 to 015 degrees True at decimal date 29.83. Radar backscatter can be influenced by shifts in the wind if the shift in direction influences wave steepness, wave breaking or the surface roughness of the wave. Radar backscatter should be

strongest in the direction the wind is coming from due to the wind dependence needed to image waves. The Hmo, wave period and wave direction during the FRF experiment are shown in figure 3.

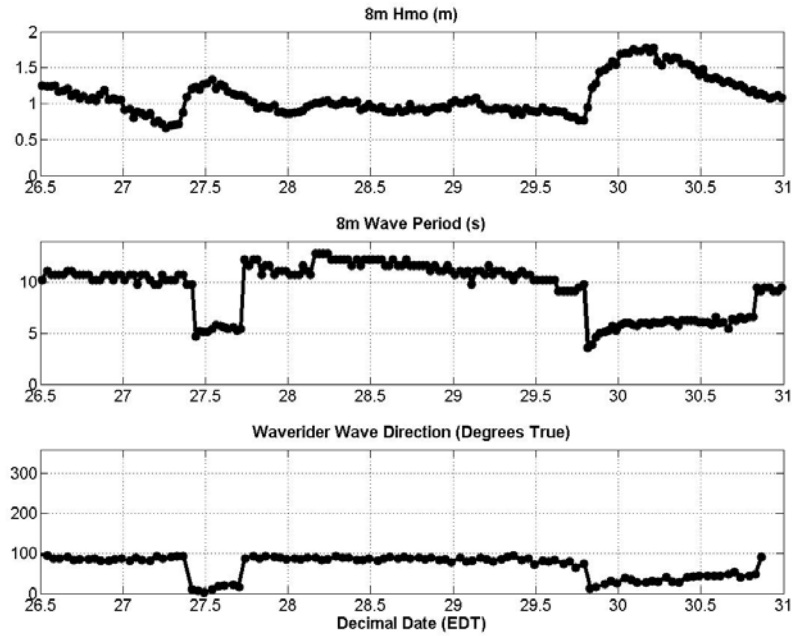

Figure 3 - Wave height (Hmo), period and direction for the FRF field deployment.

There were two significant increases in Hmo, which occurred after the two spikes in wind speed. The first occurred when Hmo increased from .67 meters at decimal date 27.3 to 1.27 meters at decimal date 27.63. The second occurred when Hmo increased from .77m at decimal date 29.8 to 1.7 meters at decimal date 30.08. Increases in wave height could produce a corresponding increase in backscatter due to tilt modulation. Shadowing of the waves will also increase as Hmo increases. Conversely, if Hmo is small enough, the small scale capillary waves will not be modulated and the ocean wave properties can not be estimated.

Decreases in wave period were observed following the two spikes in wind speed. The wave period decreased from 9.8 seconds at decimal date 27.46 to 4.7 seconds at decimal date 27.48. The wave period increased to 12.2 seconds about seven hours later at decimal date 27.78. The wave period decreased again from 9.8 seconds at decimal date 29.83 to 3.6 seconds at decimal date 29.86. The period increased slightly for the next day to 6.6 seconds at decimal date 30.86.

The wave direction shifted dramatically following the two spikes in wind speed. The wave direction shifted from 093 degrees True at decimal date 27.41 to 010 degrees True at decimal date 27.46 following the first spike in wind speed. The wave direction shifted from 074 degrees true at decimal date 29.83 to 012 degrees true at decimal date 29.87 following the second spike in wind speed. Backscatter is increased if the wave are traveling in the direction of the look angle of the radar (i.e. the radar beam is perpendicular to the wave crest). The backscatter will be significantly reduced if the wave crest is parallel to the path of radar illumination.

2.2 Marine Radar Wave Imaging System

The radar remote sensing system consisted of a Sitex RADARpc-25.9 marine X-band radar and a data acquisition computer installed with the required data acquisition software and digital receiving system. The Sitex radar was controlled through a commercial marine navigation program on a laptop independent of the data acquisition computer. The Sitex radar was mounted to the roof of the FRF office building. The data acquisition system was housed inside the office building. Data from the radar was collected hourly from the afternoon of the 26th of September, 2006, to the evening of the 30th of September, 2006, with some gaps in the data due to equipment downtime.

Table 3 contains the properties of the Sitex radar during the FRF experiment.

Property	Value
Pulse Repetition Frequency (PRF)	2000 Hz
Antenna Type	9’ Open Array
Horizontal beam width	.8°
Vertical beam width	25°
Polarization	HH
Antenna rotation speed	44 rpm
Output Power	25 kW
Pulse length	80 nsec
Inherent Range resolution	12 meters

Table 3 - Radar properties for FRF field deployment.

Several properties of the radar are adjustable. The PRF and pulselength are determined by the range setting of the radar system. The rotation speed of the antenna is determined by the sweep mode. The Sitex radar was operated in the short range with the fast sweep mode turned on**.** Additionally, the following digital collection properties can be adjusted on the data acquisition system: the digital sampling rate, the number rotations, the number of collections (triggers) per rotation, the number of samples per trigger, the number of waveforms to sum and the acquisition gate delay can be adjusted.

The digital sampling rate determines the range cell size of the radar data. It can be set to 20, 50 or 100 MHz. It is important to distinguish between the inherent resolution of the radar and the range size of the digital cell. The digital sampling rate determines the range size of the digital cell. The inherent resolution of the radar is set by the pulse length. If the inherent range resolution is 12 meters, but the range size of the cell is 3 meters, adjacent range cells are not necessarily independent. Instead it is simply sampling the footprint of the radar multiple times.

The range size for the digital cell is - $cell\ size\ in\ range\ = \frac{speed\ of\ light}{2\ \times\ sampling\ frequency}$.

The specified number of rotations determines the total collection time. The total collection time influences the frequency resolution of the spectral analysis, which will be discussed in a later section.

The number of collections determines the number of triggers that are recorded for each rotation. The number of triggers recorded determines the number of degrees digitized. The formula for calculating the average number of degrees digitally recorded per revolution is:

$$\alpha = \frac{360^{\circ}\ \times\ \#\ of\ collections}{NTR}\ \text{, where}\ NTR = \frac{PRF\ \times\ 60}{\#\ of\ waveforms\ to\ sum\ \times\ rpm}.$$

NTR is the number of average triggers per rotation.

The number of waveforms to sum determines the number of triggers that are bin averaged together. The bin averaging of triggers is done prior to digital recording of the data. The cell size

in azimuth is primarily a function of inherent radar properties, but is also affected by the number of waveforms to sum, the PRF and the rotation rate. The cell size in azimuth angle is:

$$cell\ size\ in\ azimuth\ angle\ = \frac{360^{\circ} \times rotation\ rate \times \#\ of\ waveforms\ to\ sum}{pulse\ repetition\ frequency}.$$

These digitally sampled data points along the triggers are called samples. The number of samples per trigger determines the maximum range of the digital data acquired. The maximum range is:

$$range(\max) = range\ cell\ resolution \times \#\ of\ samples.$$

It is possible for the data acquisition system to start collecting data before the triggers are actually transmitted. The area immediately surrounding the radar is inundated with backscattered electromagnetic energy. Acquisition gate delay sets the number of samples to skip before collecting data. This determines the minimum range digitally recorded and reduces noise in front of the radar. Table 4 lists the digital sampling parameters for the FRF field deployment.

Property	Value
Digital sampling rate	50 mhz
# of Rotations	640
# of waveforms to sum	8
# of samples per trigger	512
# of collections per rotation	200
Acquisition Gate Delay	0
Range Cell Size	3 meters
Azimuth Cell Size	1.06 degrees

Table 4 - Digital Sampling Parameters for FRF field deployment.

The minimum observable wavelength is determined from the inherent range resolution of the radar. The critical sampling frequency of a sinusoid is two samples per period of the sinusoid. The minimum observable wavelength is 24 meters since the inherent resolution of the radar is 12 meters. The linear dispersion relation relates period to wavelength. The linear dispersion relation

is $\sigma^2 = gk\tanh(kh)$, where $\sigma = \frac{2\pi}{T}$, $k = \frac{2\pi}{L}$, T is the wave period, L is the wavelength, g is the acceleration due to gravity and h is the water depth. Figure 4 shows that the period of a wave must increase in order to balance the linear dispersion relationship for a specified wavelength as the depth of the water decreases.

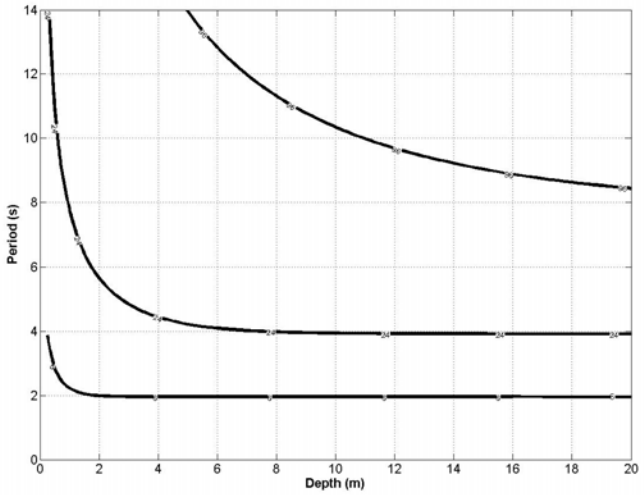

Figure 4 - The relationship of depth and period to contours of wavelength using the linear theory.

The accuracy of FFT analysis of ocean wave properties is improved if the wave conditions are statistically homogeneous. A statistically homogenous wave field is an acceptable assumption for deep water analysis, but may not be applicable for areas where refraction and shoaling are important. Trizna (2001) demonstrated that FFT analysis provides accurate results for depths as shallow as 3.7 m. Shallow water for a 24 meter wavelength is 1.2 meters.

The period as a function of water depth for a wave with a 24 meter wavelength was inversed to show the relationship of wave frequency as a function of water depth. The required sampling rate is calculated by multiplying the wave frequency by two since the critical sampling frequency of a sinusoid is two samples per period of the sinusoid. The rpm required is calculated by converting the required frequency from cycles to seconds to cycles per minute. The bottom plot of Figure 5 shows the required rpm for a 24 meter wavelength as a function of depth.

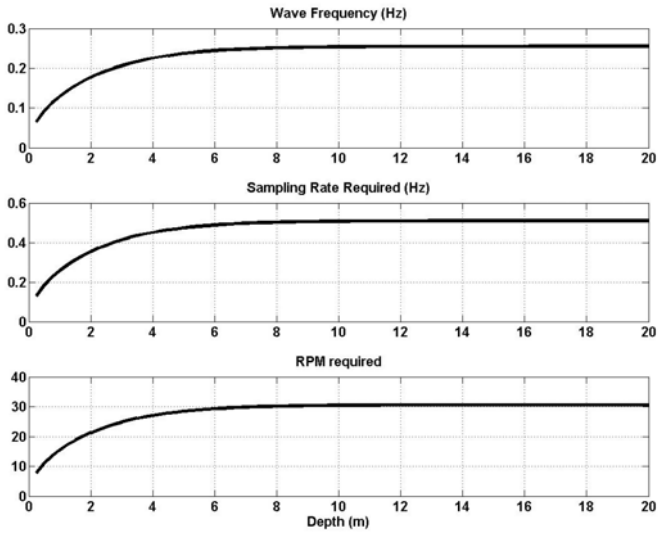

Figure 5 - The frequency, sampling rate required and rpm required for a 24 meter wave as a function of depth.

Waves with wavelengths greater than 24 meters will have smaller frequencies for a given depth. Therefore the sampling rate and RPM required will be less than what are required for a 24 meter wave. Conversely, waves with wavelengths smaller than 24 meters will have larger frequencies for a given depth. Therefore the sampling rate and RPM required will be greater than what are required for a 24 meter wave. The regular sweep mode would only allow the 24 meter wave to be imaged close to shore. Therefore, the radar should be operated in the fast sweep mode to take advantage of the inherent range resolution. Waves with wavelengths shorter than 24 meters will not be spatially resolved.

Variability in the antennae rpm was observed during data analysis even though the antenna was set to rotate at 44 rpm. The mean radar rpm for the FRF data collections was 47.6 rpm with a standard deviation of 1.9 rpm. The maximum rpm was 49.5 and the minimum rpm was 36.6. From our tests thus far it appears the variability of the rotation rate is mostly due to the wind conditions, although it is possible there may be some effects due to temperature. The radar rpm directly influences the frequency resolution and Nyquist frequency of the spectral analysis. The Nyquist frequency for Δt = 1.26 seconds is 0.397 Hz. Thus, waves with periods of 2.5 seconds or less will be aliased by this system. However, as discussed previously, this will not be of concern, since such high frequency gravity waves are shorter than the inherent spatial resolution of the imager.

The data acquisition system saves two files for every data collection. The first file contains the sequential number and the azimuth for the triggers in the data collection. In addition, the data file contains the total run time of the data collection. The file is saved as a text file with an A preceding the specific data collection date and time. The date and time is expressed with the following nomenclature - the first three digits are the Julian date, the fourth and fifth digits are the hour and the sixth and seventh are the minute. All data collections were saved in the 24 hour Eastern Daylight Savings Time (EDT) format. Therefore, the data nomenclature for a data collection at 1915 on the 28th of September is 2711915. The other file contains the raw data, which is the sample intensity as a function of range and azimuth. The raw data files were saved as binary files with an M preceding the data nomenclature describe above. The two files were later translated to Cartesian images of pixel intensity using the image processing software provided by Imaging Science Research, Inc. Since the name of the software is "Rips," the raw data images are "ripped" when they are translated to Cartesian coordinates. Figure 6 shows the Cartesian image of the 9th radar rotation of the 2711915 data collection. Areas with stronger backscatter appear white.

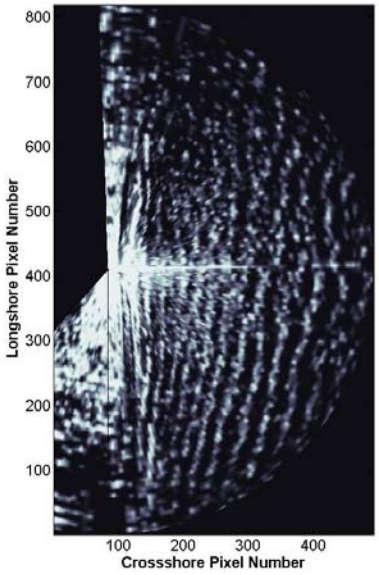

Figure 6 - Cartesian image of the 9th rotation from the 2711915 radar data collection.

The image processing software saves the Cartesian images as binary files using the collection nomenclature described above followed by the rotation number in three digit format (i.e. rotation 9 of 2711915 is saved as 2711915.009). The data analysis for the FRF field deployment was done using the Cartesian images.

The image produced by the data acquired from the radar must not vary from rotation to rotation and run to run in order to provide accurate data analysis. The possibility existed that strong variations in radar rpm caused jitter in the radar image. Therefore, the stability of the ripped images needed to be verified to ensure that pixels were located in the same place from rotation to rotation and from run to run.

The stability of the images was examined by calculating the statistics of maximum pixel intensity along a longshore transect. The longshore transect was selected at cross-shore pixel number 230 so that it would cross the FRF pier. The pier is imaged over multiple longshore pixels due to its width. The FRF pier was visually observed between pixel numbers 411-415 during data analysis. Therefore, the search along the longshore transect was limited to longshore pixel numbers 401 and 425 so that the pixel with the maximum intensity would most likely be the FRF pier.

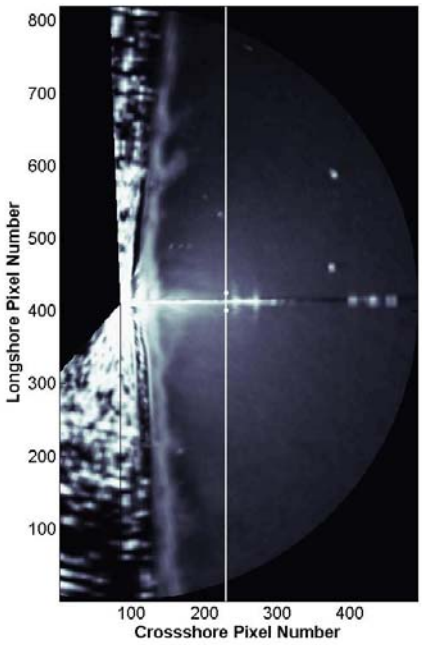

Figure 7 - Longshore transect used to quantify pier stability overlaid on 271195 mean pixel intensity image.

Figure 7 shows the mean pixel intensity image for the 2711915 data collection. The longshore transect used is visible as the vertical white line. The upper and lower bounds for the maximum pixel intensity are white dots plotted on the longshore transect that appear above and below the pier. The FRF pier is the bright white line that is parallel to the x axis in the middle of the image.

The mean, median and standard deviation of the pixel number at which the maximum pixel intensity occurred along the longshore transect for all 640 rotations were calculated for each run. The results are summarized by the two histograms displayed in Figure 8. The histogram on the left shows the distribution of the mean maximum pixel intensity calculated from each run. The histogram on the right shows the distribution of the standard deviation of the maximum pixel number from each run.

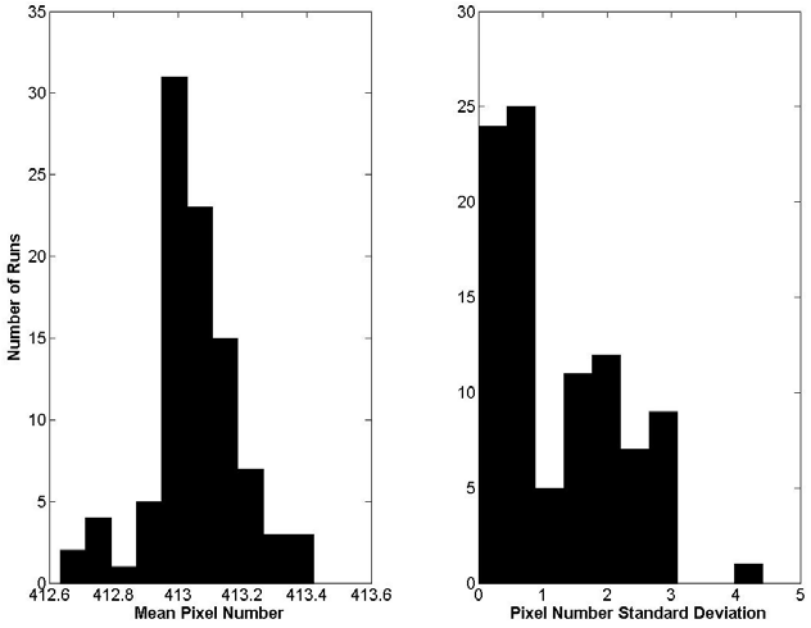

Figure 8 - Histograms of mean maximum pixel intensity and standard deviation of maximum pixel intensity for every data collection.

The mean of the maximum pixel number stays within +/- 1 pixel of the pier for the FRF experiment assuming that pixel number 413 is the center of the FRF pier. The average standard deviation of the location of the maximum pixel intensities is 1.2 pixels. However, several runs exhibit much higher standard deviations. These high standard deviations are believed to be caused by strong wave backscatter, since visual observations of the data showed no significant shift in the location of the pier.

A 2 rotation average was used to examine if the high standard deviations were caused by the ocean wave backscatter or radar jitter. The 2 rotation average was used to remove any strong wave backscatter through temporal averaging. The histograms of the bin averaged mean and standard deviation of the maximum pixel intensity are shown below.

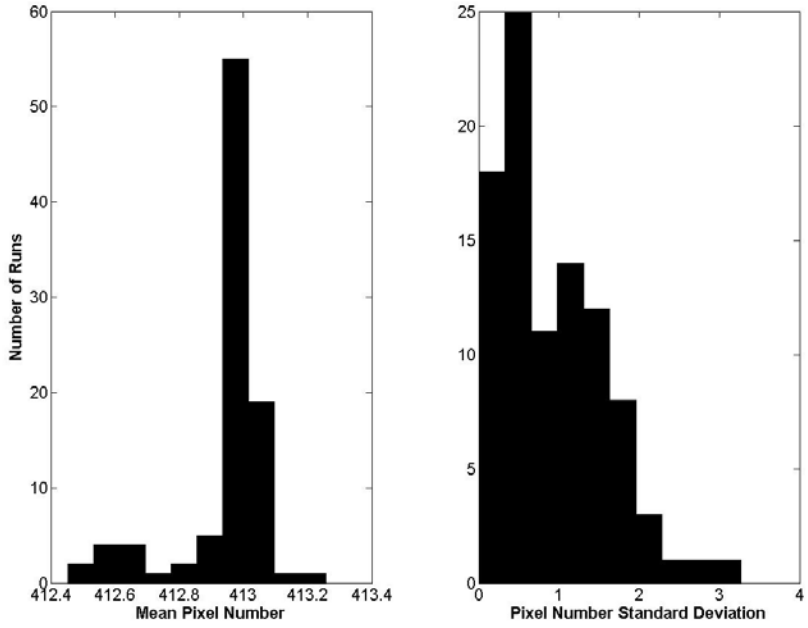

Figure 9 - Histograms of mean maximum pixel intensity and standard deviation of maximum pixel intensity for every data collection using a 2 bin rotation average.

As expected the average standard deviation is reduced from 1.2 to .9250 pixels. Therefore it is believed that jitter causes a slight variation in the radar image. However, this variation will be ignored since it is less than one pixel. Table 5 summarizes the statistics discussed above.

Property name	Value
Pixel number maximum	
Average mean	413.1
Average median	413.0
Average standard deviation	1.2
Averaged pixel number maximum (bin size equals 2 revolutions)	
Average mean	413.0
Average median	413.0
Average standard deviation	.93

Table 5 - Statistics for the maximum pixel number along a longshore transect.

The RIPS software generates images with uniform spatial grids based on the range resolution set by the digital sampling rate. The radar coordinate system needs to be transformed to the FRF coordinate system in order to correctly identify locations in the radar image. The FRF coordinate system is a uniform Cartesian grid of x (cross-shore) and y (longshore) coordinates. The origin of the FRF coordinate system is the intersection of a shore-parallel baseline with the southern boundary of the FRF property. Positive directions are toward the north (longshore) and offshore (cross-shore). The FRF pier is parallel to the cross-shore axis.

No rotation of the radar image is required to transform the RIPS coordinate system to the FRF coordinate system, since the pier is parallel to the x-axis in the radar image. Additionally, the images from the Rips software were shown to be to be sufficiently stable for analysis in the previous section. Therefore, the geo-location of the radar image requires only a uniform translation to geo-locate the radar images. The geo-location of the radar image was accomplished through the use of several ground control points (GCPs) identifiable in both the FRF coordinate system and the radar coordinate system.

The position of the radar on the FRF office building and the locations of some instrument towers along the FRF pier were surveyed by hand held GPS. The GPS coordinates were converted to FRF coordinates by a member of the FRF Staff (Kent Hathaway). The FRF coordinates of the surveyed points are posted in the Table 6. The sources of surveys are also posted in Table 6. Additionally, coordinates from the FRF website for Anemometer 3932, which is located on the tower at the end of the pier, are listed in the table below in order to qualitatively quantify the accuracy of the hand held GPS coordinates for the tower at the end of the pier.

Name	FRF Cross-shore (m)	FRF Longshore (m)	Survey Source
Radar	31.21	518.33	Hand held GPS
SIS Tower	517.40	513.25	Hand held GPS
NOAA Tower	567.01	510.61	Hand held GPS
Tower (EOP)	600.08	505.62	Hand held GPS
Anemometer 3932	585.20	517.30	USACE

Table 6 - FRF coordinates of radar and GCPs

The position for the tower at the EOP surveyed by the hand held GPS is about 15 meters away from the published FRF position of Anemometer 3932. This is not a surprise, though, because the hand held GPS is only accurate within five to ten meters. Additionally, the positions will be different because the point surveyed by hand held GPS does not correspond exactly to Anemometer 3932.

Distances were calculated between the radar and the points of interest in the table above using FRF coordinates. The distance results are posted in Table 7. These distances will be used to verify the uniform translation of the geo-location.

Item	Distance from Radar (m)
Base of SIS tower	486
Base of NOAA tower	536
Tower EOP	569
Tower EOP (USACE)	554

Table 7 - Distances towers and radar using FRF coordinates.

To verify the uniform translation, the distances calculated from FRF coordinates were related to distances calculated from ground control points (GCPs) in the radar images using the pixel coordinate system. The pixel coordinate system of the radar images contains 819 longshore pixels and 493 cross-shore pixels. The origin of the pixel coordinate system is in the lower left hand corner of the image. Longshore pixel numbers increase going north and cross-shore pixel numbers increase going offshore. The radar is located at cross-shore pixel number 84 and longshore pixel number 410 in the pixel coordinate system.

The mean pixel intensity radar image in figure 10 shows six strong radar returns in line with the radar. These returns will be used as the GCPs. The GCPs are numbered according to their relative cross-shore location (i.e. GCP 1 is closest to the radar and GCP 6 is furthest from the radar). The six GCPs are clearly observable in the mean pixel intensity radar image for the 2711915 data collection. The radar location, GCP 1 and GCP 2 are circled.

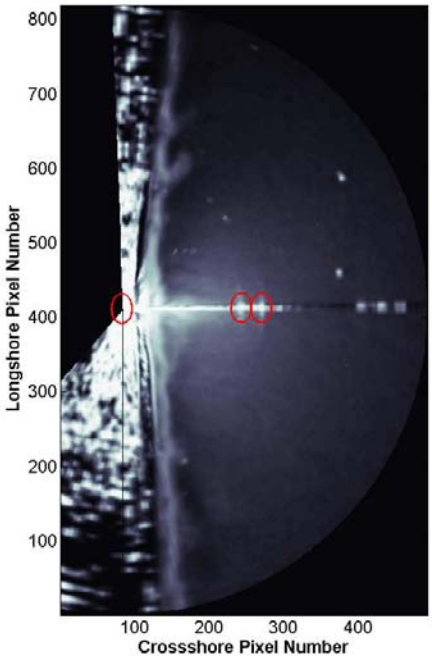

Figure 10 - Locations of radar, GCP 1 and GC 2 identified on 2711915 mean pixel intensity image.

Originally, GCP 3 was assumed to be the end of the pier. However, after calculating the distances to each GCP it was later assumed that GCP 3 is caused by the end of the pier being smeared by the inherent range resolution of the radar. GCPs 4, 5 and 6 are assumed to be "double bounces" of the first three GCPs. A double bounce occurs when the trigger from the radar is reflected off the target back towards the radar, reflected to the target again and finally reflected back to the antenna. The travel time is twice what it would normally be if the trigger traveled directly between the radar and the target in a double bounce. Thus the target appears two times farther away than it should. The pixel coordinates and distances from the radar for GCP 1 and GCP 2 using a Δx and Δy of 3 meters are posted in the Table 8.

Item	Pixel Coordinates		Distance From Radar
	Cross-shore	Longshore	(m)
Radar	84	410	n/a
Target 1	249	413	495
Target 2	274	413	570

Table 8 - Distances calculated in the pixel coordinate system using a Δx and Δy of 3 meters.

The distance from the radar to the tower at the end of the pier using the FRF coordinate system (569 m) agrees extremely well with the distance between the radar and GCP 2 using a Δx and Δy of three meters (570 m). Based on the calculated distances, GCPs 1 and 2 are believed to be the SIS tower and the tower at end of the pier respectively. The difference in distances between the SIS tower and the radar for the FRF and pixel coordinate system could be explained by a different position of the SIS Tower providing the source of backscatter than the point surveyed for the SIS Tower. Therefore, a uniform translation using a known coordinate for a GCP and a Δx and Δy of three meters can be used on the radar image.

2.3 Results

Peak Period

A 3D datacube of pixel intensity timeseries representing each pixel in a given data window were created by loading each of the 640 Cartesian image files (one per rotation) into MATLAB. The three dimensions of the 3D data cube correspond to the longshore pixel number, the cross-shore pixel number and rotation number of the radar, respectively. Each pixel time series was windowed and Fourier transformed individually, and spectral quantities were summed and averaged across all the pixels to increase the degrees of freedom.

The frequency resolution, Δf, is determined by the record length, N, used for spectral decomposition and the Δt of the radar. The formula for calculating the frequency resolution is $\Delta f = \frac{1}{N\Delta t}$. For the following spectral analysis in the frequency domain we used 10 ensembles of 64 points each (i.e. $N = 64$). Thus, the frequency resolution was Δf = 0.012 Hz.

Two 64 pixel x 64 pixel data windows were used for spectral decomposition in the frequency domain. Figure 11 shows the data windows used for analysis of peak period overlaid on the mean pixel intensity radar image for 2711915.

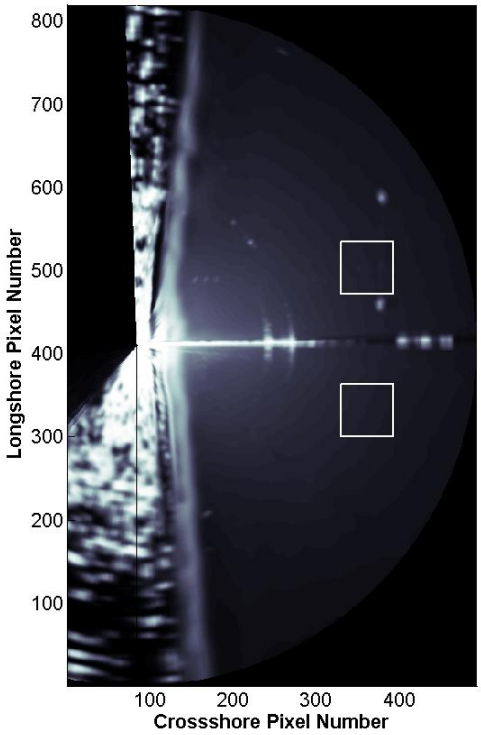

Figure 11 - Data windows used for analysis of Peak period

Table 9 lists the pixel and FRF coordinates of the data windows.

64 x 64 pixel data window	Pixel Coordinates	FRF Coordinates
Northern Data Window		
FRF Longshore (min)	472	704
FRF Longshore (max)	535	893
FRF Cross-shore (min)	330	757
FRF Cross-shore (max)	393	943
Southern Data Window		
FRF Longshore (min)	300	194
FRF Longshore (max)	363	380
FRF Cross-shore (min)	330	757
FRF Cross-shore (max)	393	943

Table 9 - Pixel and FRF coordinates of data windows used to analyze peak period.

Ensemble averaging was used to obtain the peak period for each radar data collection. Ensemble averaging smoothes the spectral decomposition by averaging the Fourier coefficients of multiple time series created from the original time series at the cost of decrease in frequency resolution. The periodicity of the radar data is observable from the partial plot of a pixel intensity time series in Figure 12.

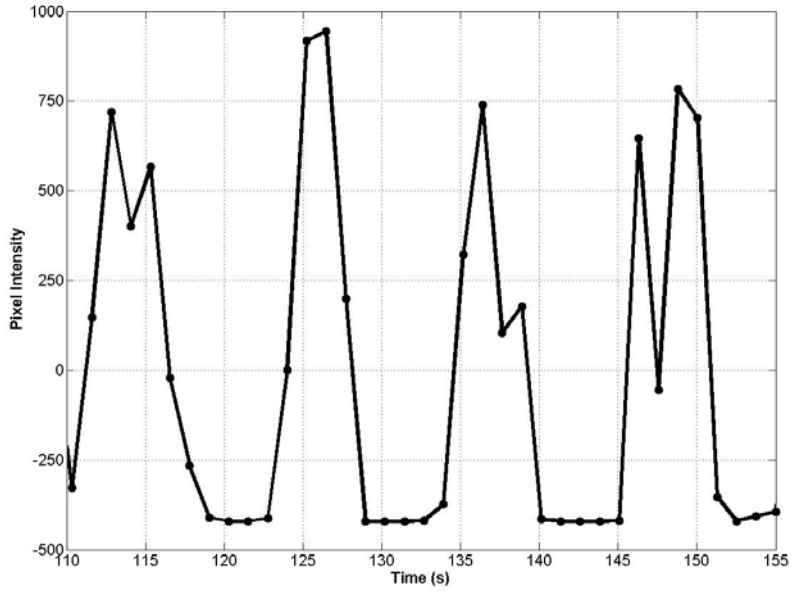

Figure 12 - Partial plot of a pixel intensity time series.

Data analysis was carried out one pixel at a time for every pixel in the data window. Data analysis began by splitting the 640 point pixel intensity time series into ten time series with 64 points each. The ten time series were demeaned then tapered using a Hanning data window. The variance of time series was preserved by multiplying the FFT of the time series by a ratio of original to tapered timeseries variance. The mean of the ten variance preserved FFTs represents the ensemble averaged FFT. The two sided PSD was produced by multiplying the ensemble averaged FFT by its complex conjugate and normalizing by the record length multiplied by Δt. The one sided PSD was created from the two sided PSD by extracting the spectral powers for positive frequencies greater than the zeroth frequency and less than the Nyquist frequency. The spectral power for the one sided PSD was doubled to account for the spectral power in the negative frequencies. The peak frequency was obtained from the one sided PSD by locating the Fourier frequency with the maximum spectral power. The minimum peak frequency was hard

coded to the fourth Fourier frequency, which corresponded to a period of approximately 20 seconds. The minimum frequency value varies slightly due to the variation in RPM from collection to collection. The variation is accounted for in each collection by calculating the Fourier frequencies based on the rpm calculated for the collection. The peak period is calculated by taking the inverse of the peak frequency.

The process described above was repeated for every pixel in the data window. Matrices of peak frequency for every pixel in the data window were created for each radar data collection. A matrix of energy was also calculated by multiplying the sum of the spectral power for the two sided PSD by Δf .

The average peak frequency, fpeakavg, was calculated by taking the mean of the peak frequency for every pixel. The standard deviation, fpeakstd, and average peak period, Tpeakavg, were also calculated from the matrix of peak frequencies. The peak frequency was also obtained by summing the PSDs for every pixel and picking off the Fourier frequency with the greatest spectral power. This value is reported as fpeakpsd. The minimum fpeakpsd is limited to the fourth Fourier frequency as previously discussed. Finally, the energy was calculated from the summed PSD by multiplying the sum of the spectral power for summed PSD by Δf . The spectrum below shows the summed PSD for the data collection at 2711915. The spectrum is plotted on a partial log plot.

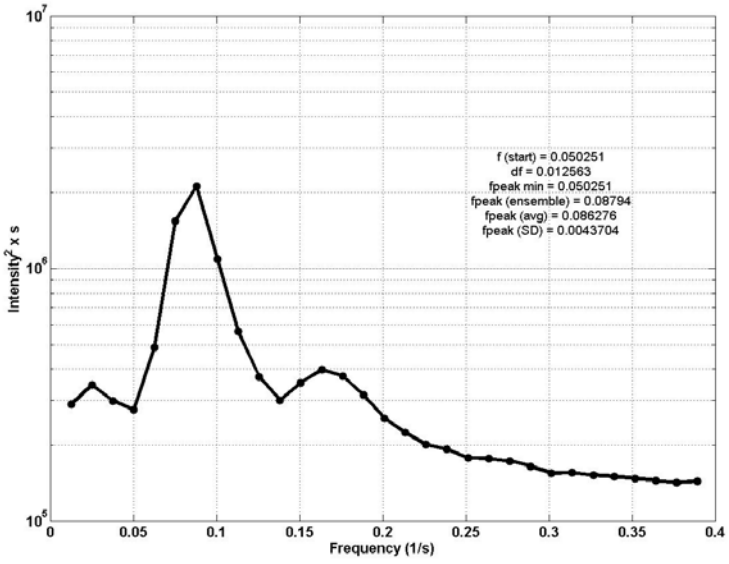

Figure 13 - Power spectral density for 2711915 radar data collection.

The peak period data acquired from the radar agrees well with the FRF in-situ sensors. The results of the radar peak period for the FRF field deployment are visible in the figure below.

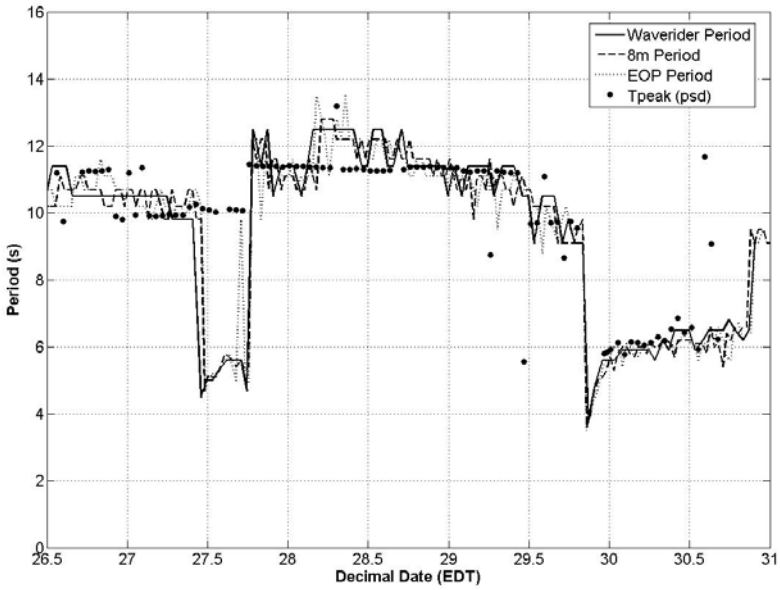

Figure 14 - Estimated wav e period from radar compared to in situ wave period.

There was only one interval where the period observed by the radar is significantly different than the in situ sensors. This interval was from decimal date 27.47 to decimal date 27.76. There were also four runs that showed a significant difference between the period observed by the radar and the in situ sensors. The four runs are decimal dates 29.26, 29.47, 30.59 and 30.64.

The PSDs for decimal dates 27.47 to 27.76 contain two significant peaks, indicating that there was a strong high frequency component to the sea state. The high frequency peak of the spectrum is most likely from short wind waves generated by strong winds. The periods of the second peak for range from 5.1 to 6.2 seconds for decimal dates 27.47 to 27.76. The FRF in-situ sensors periods range from 4.5 to 5.1 seconds during the same interval. Figure 15 shows the PSD computed for the 27.47 decimal date radar data collection.

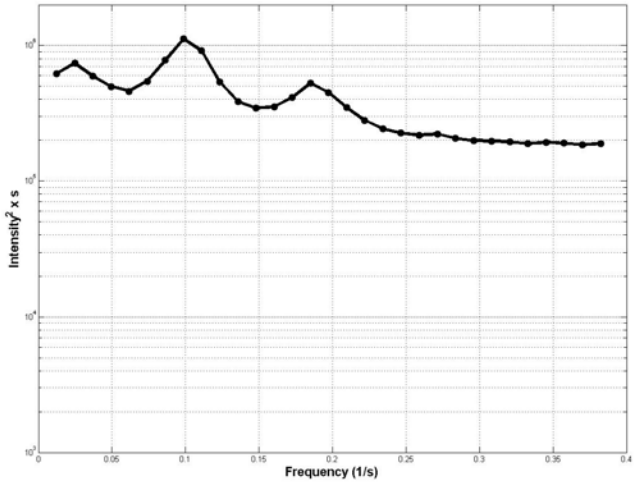

Figure 15 - PSD for the 27.47 radar data collection.

The period of the second peak in for the PSD displayed in Figure 13 is 5.4 seconds, which closely aggress to the FRF in situ period of 5 seconds. The first spike in wind speed preceded the bimodal spectrums by an hour. The spectrums lost their high frequency peaks when the wind speed droped below 8 m/s at 27.76. Bimodal spectrums were observed again when the wind speed spiked at 29.8.

The PSD for 29.26 is displayed in Figure 16. The PSD calculated for the 29.26 decimal date radar collection was flat. It is believed that the wind velocity was not strong enough to produce the surface roughness required to properly image the ocean waves. The wind speed at decimal date 29.26 was less than four meters per second. The PSD calculated for 29.47 was also flat. The wind speed at 29.47 was 2.8 m/s. Further examination revealed that the interval from decimal date 29.14 to 29.76 contained only flat PSDs. The wind speed ranged from 1.9 to 5.3 m/s during the interval from decimal date 29.14 to 29.76.

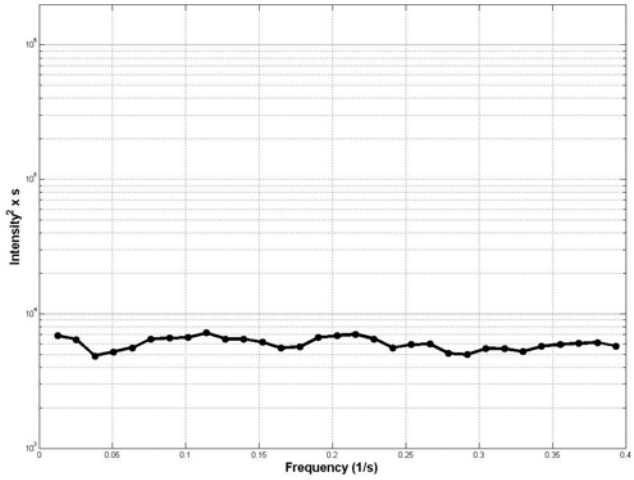

Figure 16 - PSD for the 29.26 decimal date radar collection.

These intervals where the radar does not accurately predict the period can be correlated to variations in image energy. Figure 17 is the partial logarithmic plot of image energy for each data collection during the FRF field deployment.

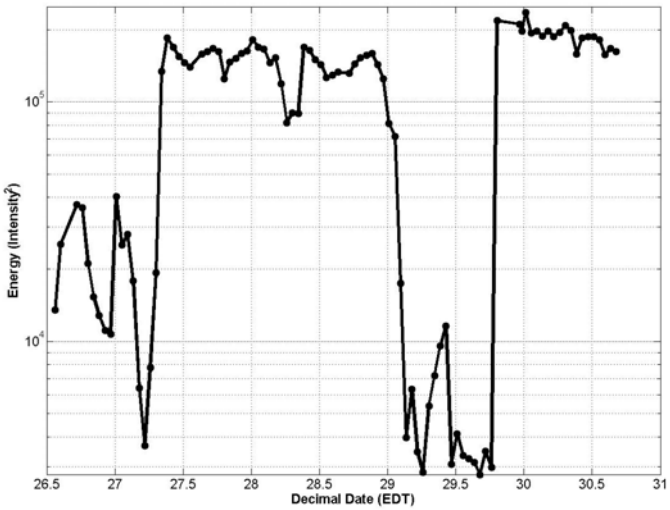

Figure 17 - Partial logarithmic plot of image energy for MCR field deployment.

Spikes in energy are visually correlated with the spikes in the wind speed. Additionally, the period where the wind spectrums are flat correlates well with the period of minimum energy.

Spatial variation of period

Figure 18 shows the peak period for every pixel inside a 400 x 200 pixel data window for the 2710215 (decimal date of 28.09) data collection. The peak period map is overlaid on top of the mean pixel intensity in Figure 18.

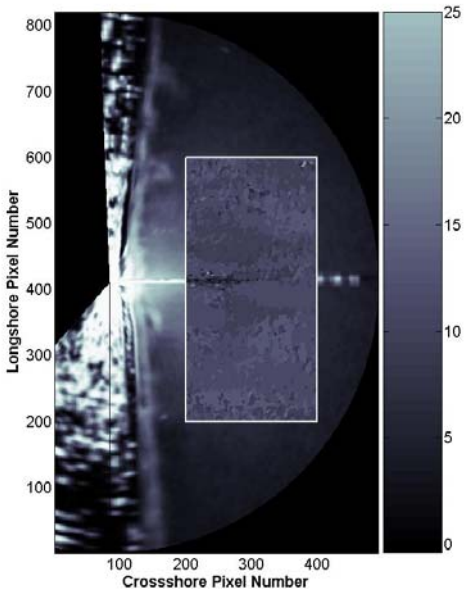

Figure 18 - Period map overlaid on top of mean pixel intensity for the data collection at decimal data 28.09.

The periods in the data window range mostly from 9 to 13 seconds. There are several areas of periods in the data window that would not be expected for normal gravity waves. These are probably due to backscattering mechanisms that are not fully understood and the spectral decomposition of pixels that contain deployed instruments or the portions pier. Areas with periods outside of the range of a normal gravity wave are increased when the radar is not pointed in the direction of the incoming waves. This is seen in figure 19 when the data window is extended to cover a larger area of the radar image. Notice how the areas to the upper and lower left of the data window have a lot of period variability.

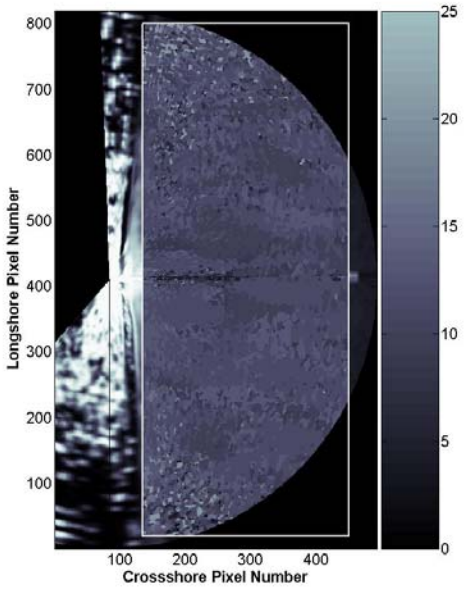

Figure 19 - A lager period map overlaid on the mean pixel intensity for the data collection at decimal data 28.09

Figure 20 shows the standard deviation of the estimated period for each collection. Intervals of low wind speed correlate well with intervals of high standard deviation. This is clear where the wind speed stays below 5.3 m/s for the period of 29.0 to 29.75.

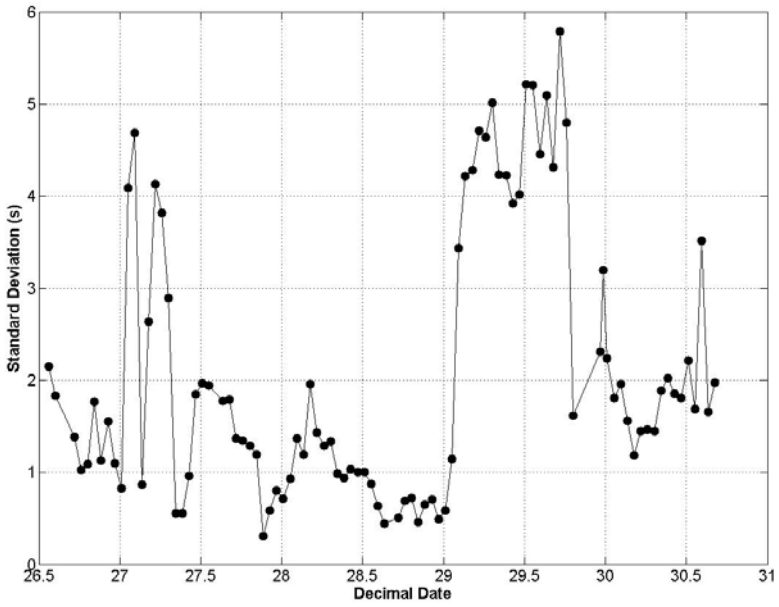

Figure 20 - Standard deviation of estimated periods from each run.

Dominant Direction

The 2D PSD was used to estimate dominant direction from the radar data. A relative coordinate system that mirrors the FRF pier and coast orientation was used to easily convert degrees relative to degrees true. The relative coordinate system is orientated with the x-axis shore normal to the coast. Therefore, 0 degrees relative (R) is along the x-axis and the coast is along the y-axis. Positive angles are measured counterclockwise from the x-axis and negative angles are measured clockwise from the x-axis. The coordinate system was split into quadrants to facilitate data analysis. Quadrant 1 encompasses 0 to 90 degrees R, quadrant 2 encompasses 91 to 180 degrees R, quadrant 3 encompasses -180 to -91 degrees R and quadrant 4 encompasses -90 to 0 degrees R. Since the FRF pier is aligned along 072˚ True (T) in the True North coordinate returned from quadrant 1 will be subtracted from 072˚ T and angles from quadrant 4 will be added to 072˚ T to obtain the True direction.

The wave surface in Figure 21 was generated using the equation $\eta(x,y) = A \times \cos(k_x \cos(\theta)x + k_y \sin(\theta)y)$, where $\theta = 60^\circ$, A = 1 and $k_x = k_y$. The wave surface was created over 64 pixels in the x and y direction. The spacing between the pixels in the x and y direction is 3 meters (i.e. $\Delta x = \Delta y = 3$ meters). This wave is approaching the coast at 60° R in the relative coordinate system.

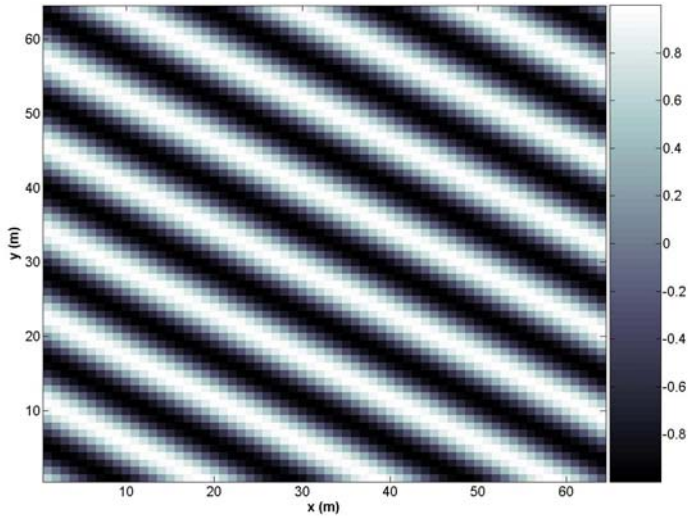

Figure 21 - An Artificially generated wave surface propagating towards the coast. The coast is to the left of the image and perpendicular to the x axis.

The quadrants of the relative coordinate system are shown on the 2D PSD of the artificially generated wave in Figure 22.

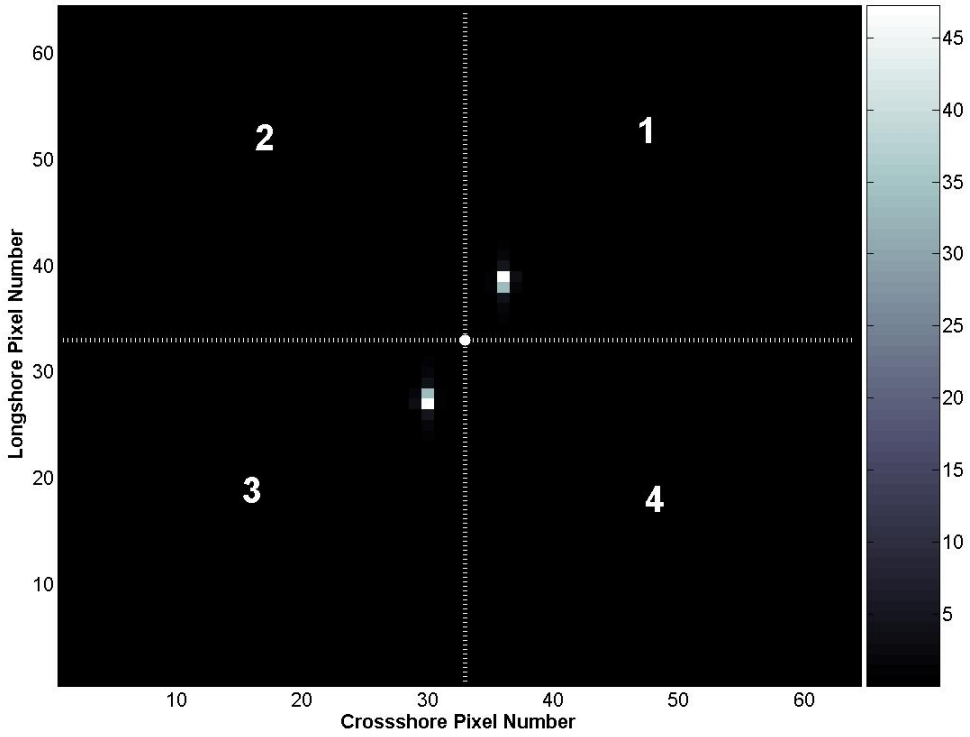

Figure 22 - 2D PSD of the artificially generated wave surface. Quadrants used in data analysis are identified.

To determine the dominant direction the maximum spectral power for each quadrant is identified. Only the maximum of the spectral power for quadrants 1 and 4 will be compared since they represent a wave propagating towards the coast in this relative coordinate system. It is obvious from Figure 22 that the maximum spectral power for quadrant 1 is greater than the maximum for quadrant 4. The relative dominant angle, θ, is calculated from $\theta = \tan^{-1}\left(\frac{k_y(\max)}{k_x(\max)}\right)$. The column and row location of $k_x(\max)$ and $k_y(\max)$ in the 2D PSD give the information needed to quantify the wave numbers and calculate the dominant direction. To help illustrate this process, transects of the row corresponding to $k_x(\max)$ and the column corresponding to $k_y(\max)$ are extracted from the 2D PSD. The transects are identified on the 2D PSD by the dotted white lines in Figure 23.

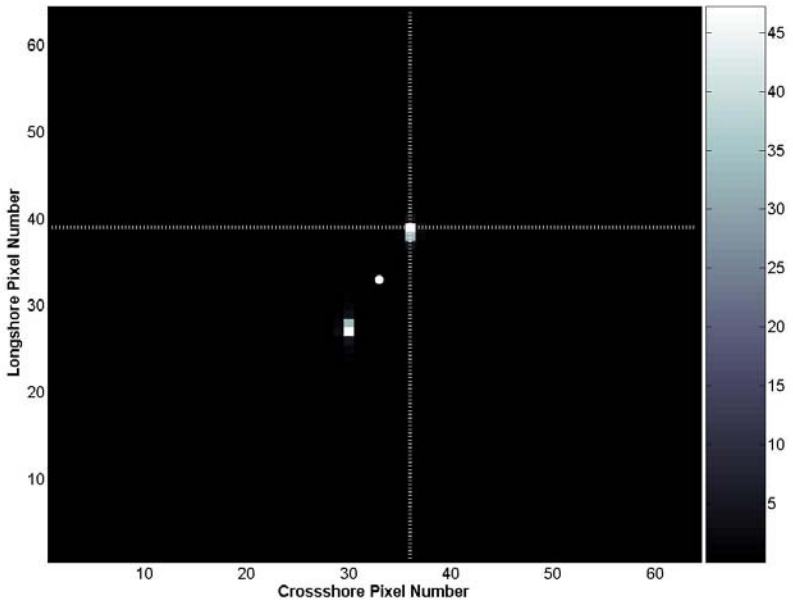

Figure 23 - Transects along maximum x and y wave numbers.

The transects of the 2D PSD are 1D PSDs in the x and y wavenumber space. The 1D PSDs for $kx(\max)$ and $ky(\max)$ are shown in the Figure 24.

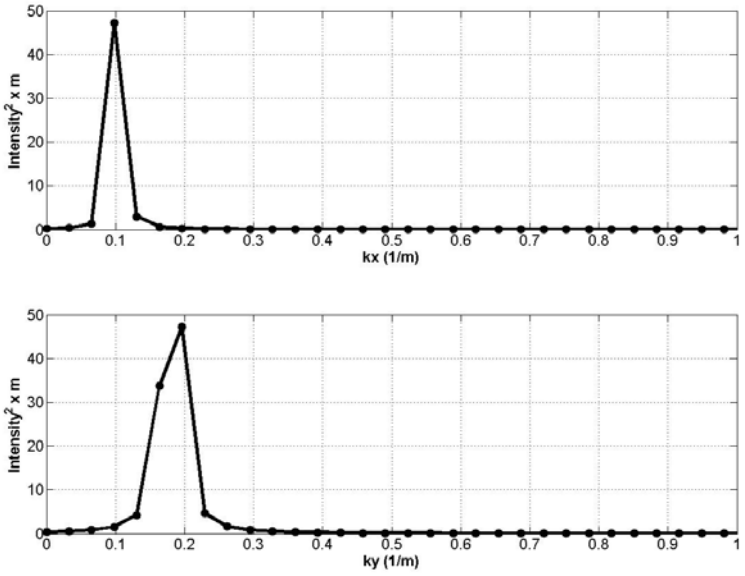

Figure 24 - 1D PSDs from transects on the 2D PSD. Maximum wave numbers in the x and y direction are identified by finding the wavenumber with the maximum spectral power.

The angle returned from the arctangent of the ratio of $k_y(\max)$ to $k_x(\max)$ is 63.4°. The True North angle is calculated as discussed previously be subtracting 63.4° R from 072° T. Thus, the wave is coming from 8.6° degrees True.

Two different size data windows were used to calculate wave direction. One was 128 x 128 pixels and the other was 64 x 64 pixels. The data windows were 384 meters and 192 meters on a side, respectively, based on a Δx and Δy equal to 3m. The advantage of using the larger data window was an increase in wavenumber resolution. The larger data window provided a Δk that was half the magnitude of the smaller window. The formula for the x wavenumber resolution is $\Delta k_x = \frac{2\pi}{N_x \Delta x}$, where N represents the number of pixels in the x direction in the data window and Δx represents the distance between the pixels. The formula for the y wavenumber resolution is $\Delta k_y = \frac{2\pi}{N_y \Delta y}$. The wavenumber resolution and the FRF coordinates of the two data windows are posted Table 10.

128 x 128 Pixel Data Window	Pixel Coordinate	FRF Coordinate
FRF Longshore (min)	268	89
FRF Longshore (max)	395	473
FRF Cross-shore (min)	320	736
FRF Cross-shore (max)	447	1120
k resolution (x, y, total)	.0164 m^{-1}, .0164 m^{-1}, .0082 m^{-1}	
64 x 64 Pixel Data Window	Pixel Coordinate	FRF Coordinate
FRF Longshore (min)	332	281
FRF Longshore (max)	395	473
FRF Cross-shore (min)	407	997
FRF Cross-shore (max)	470	1189
k resolution (x, y, total)	.0327 m^{-1}, .0327 m^{-1}, .0164 m^{-1}	

Table 10 - Pixel and FRF coordinates of data windows used to analyze dominant direction

Figure 25 shows the location of the two data windows. The 64 x64 window is the smaller box further offshore.

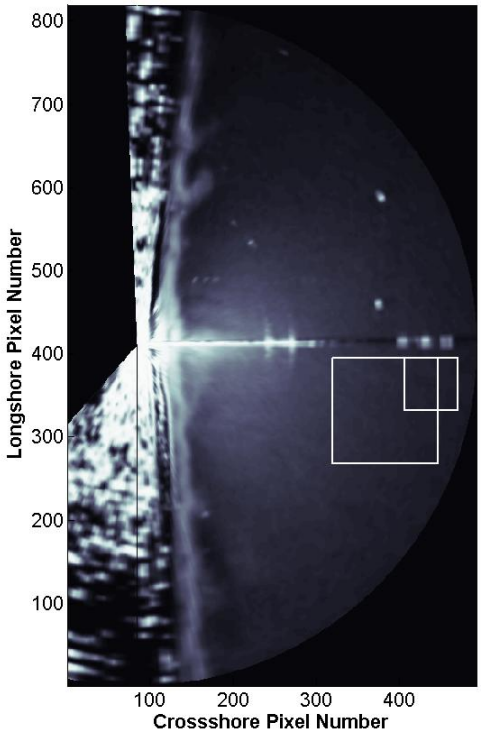

Figure 25 - Location of data windows used to obtain dominant wave direction.

A 3D datacube of pixel intensity images in a given data window were created by loading each of the 640 Cartersian image files (one per rotation) into MATLAB. The images within the data windows were then analyzed using the methodology for estimating the dominant direction as previously discussed. The mean of the 640 dominant directions was saved as the average dominant direction for the each data collection.

The following is an example of the estimation of wave direction from one rotation of 2711915 FRF radar data collection. Figure 26 shows the 128 x 128 pixel data window plotted on the image for one rotation of the 2711915 data collection.

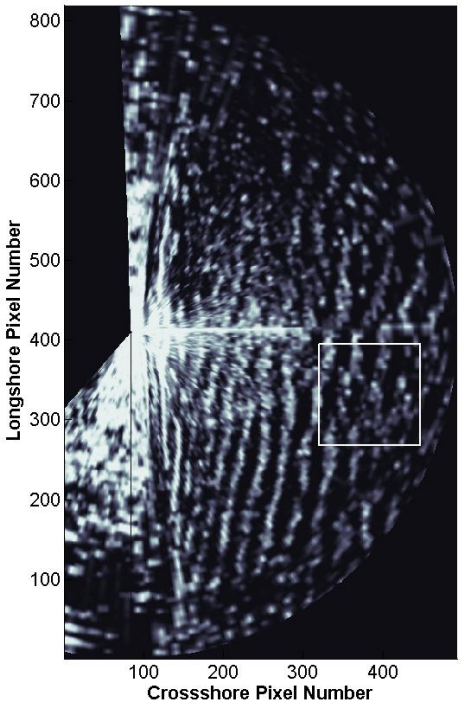

Figure 26 - 128 x 128 data window overlaid on image of single radar rotation.

A close up of the image in the data is shown in Figure 27.

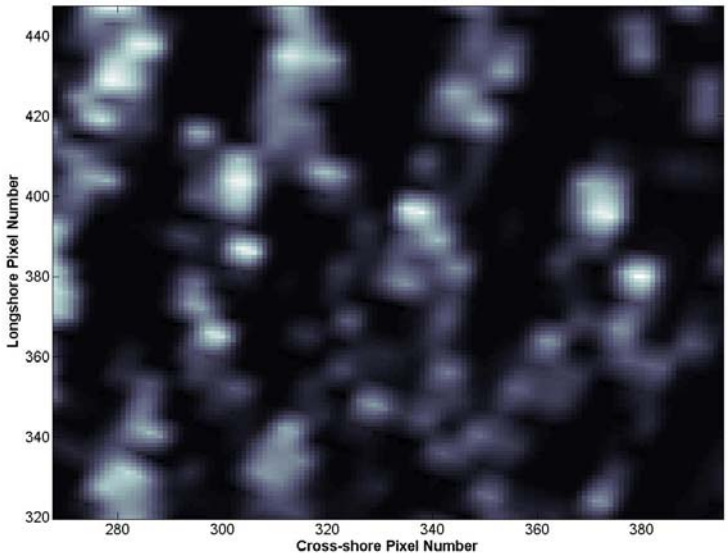

Figure 27 - Image contained in data window of figure 26.

The 2D PSD for data window for one revolution of the 2711915 data collection is shown in Figure 28.

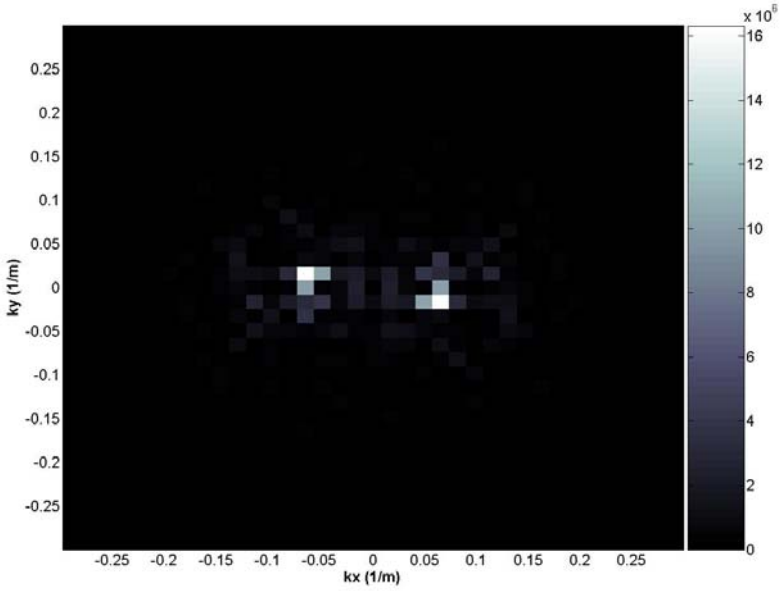

Figure 28 - 2D PSD of 128 x 128 data window using FRF data

The one sided $k_x(\max)$ and $k_y(\max)$ PSDs are shown in Figure 29.

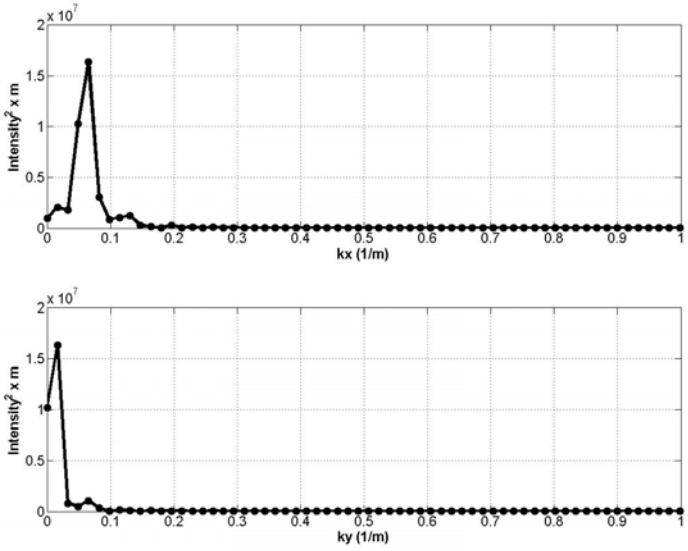

Figure 29 - One sided PSDs for $k_x(\max)$ and $k_y(\max)$

The angle computed for the example rotation of 2711915 is 14 degrees. The relative angle is added to 86˚ True since the maximum occurs in quadrant 4. The average dominant angle for all 640 revolutions using a 128 point data windows is 84.8˚ T and the average peak angle using all 640 64 point data windows is 82.5˚ T. The wave rider buoy reports the wave direction for 2711900 as 089˚, which agrees well with the dominant wave direction obtained from the radar data. Figure 30 shows the dominant wave direction estimated for each data collection from the FRF field deployment.

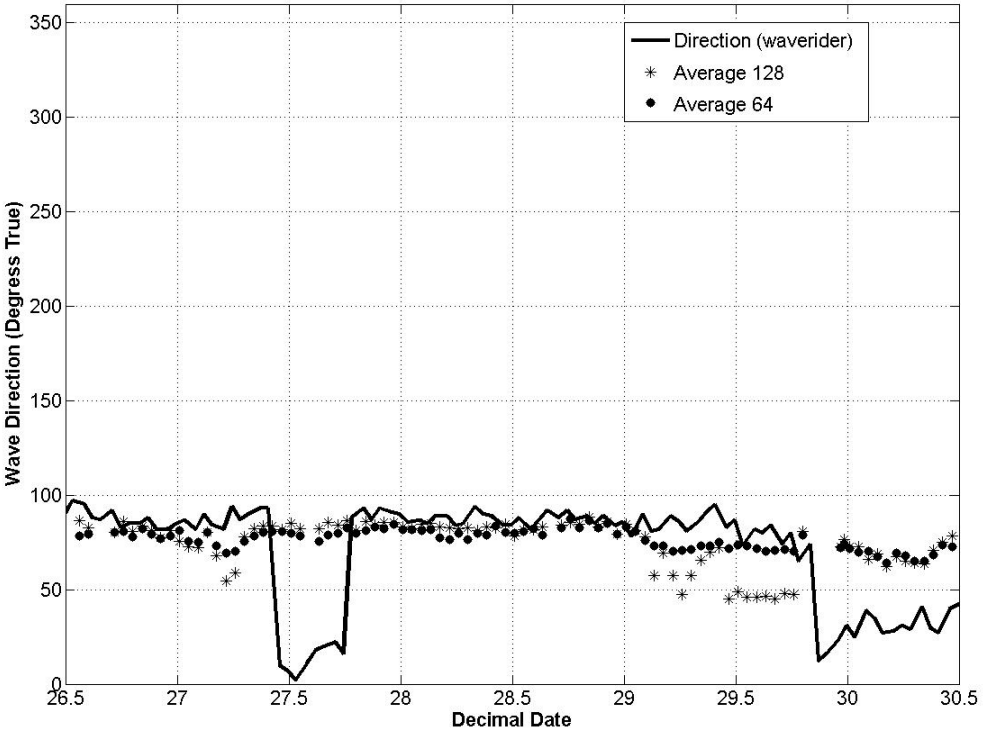

Figure 30 - Estimated dominant wave direction from the radar compared to in situ wave direction.

There is little variation of the wave direction obtained from the radar for the 64 x 64 window. The 128 x 128 shows some variation during periods of decreasing wind speed and low image energy. This is seen quite clear from the interval of decimal date 29.14 to 29.76. The location of the data window compared to the in situ sensor used to obtain wave direction may be the cause for the difference in wave directions acquired from the data windows, since waves orient themselves towards shore normal as the approach the coast. The wave rider buoy used to wave directions at the FRF is almost 4 km away from the center of the two data windows. Wind waves

would be free to travel in any direction further offshore, but towards the coast were the data window was used waves orienting themselves shore normal would dominate.

3. Field Deployment II

3.1 Field Site

The autonomous radar remote sensing system was tested at the Mouth of the Columbia River from the 16th to the 19th of January 2006. The system was set up on Benson Beach, just north of the North Jetty of the Mouth of the Columbia River. Temporary scaffolding and sand anchors were used to create a stable platform for the radar. The data acquisition system was stored inside a suburban, which was parked close to the scaffolding. A portable propane generator was used to power all electronic equipment. The generator was housed in a mobile trailer. Figure 31 shows a picture of the set up for the MCR field deployment.

Figure 31 - X-band remote sensing system set up for the MCR field deployment.

Data collections began on the 16th of January at 1805 and ended on the 19th of January at 1805. The generator and data acquisition system were checked periodically to ensure proper operation. Data collections were conducted hourly except during equipment downtimes.

The nearest source of meteorological and wave data is NOAA Buoy 46029, which is located 21 nautical miles southwest of the Mouth of the Columbia River. The atmospheric pressure, wind speed and wind direction are shown in figure 32.

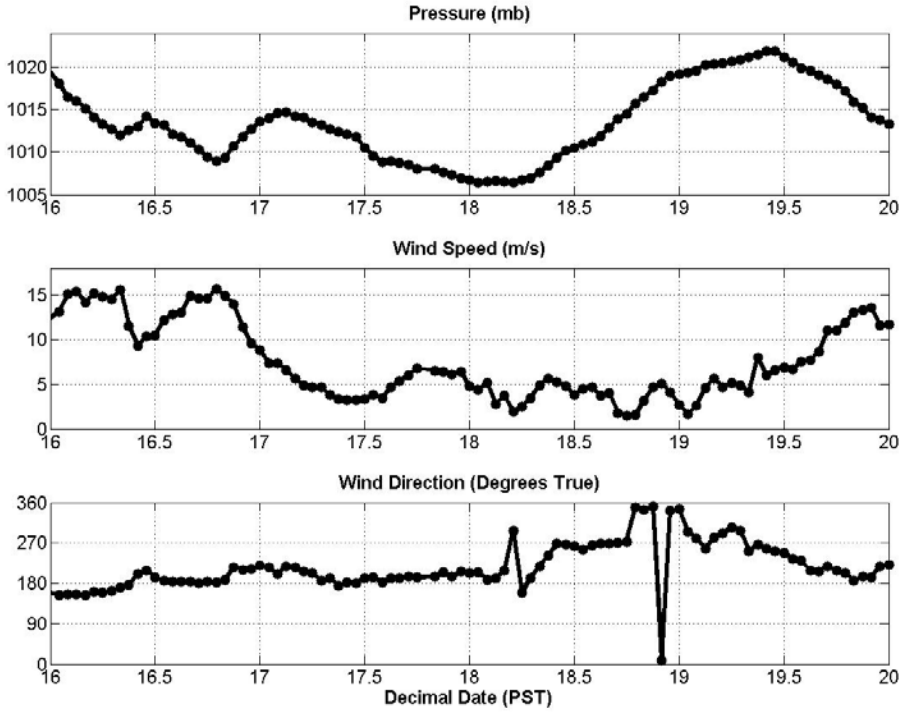

Figure 32 - Atmospheric pressure, wind speed and wind direction for the MCR field deployment.

There were three recorded drops in pressure from the 16th to the 20th of January 2006 at NOAA NDBC Buoy 46029. The lowest pressure of the first drop occurred at decimal date 16.33. The pressure increased slightly then bottomed out again at decimal date 16.79, which is about an hour after the first MCR radar data collection. The pressure increased again then steadily dropped to the lowest pressure recorded during the experiment at decimal date 18.04. The pressure held steady for about four hours then gradually increased to the highest recorded pressure during the experiment at decimal date 19.42. After which the pressure decreased for the remainder of the experiment.

The wind speed spiked after the first two drops in pressure. The first peak in wind speed occurred at decimal date 16.83 and the second peak occurred at decimal date 16.79. The wind speed steadily decreased from its peak at decimal date 16.79 to 3.4 m/s at decimal date 17.38. The wind speed remained light and variable for the next two days. There were no significant increases in wind speed when the pressure dropped for the third time. The wind speed gradually increased from decimal date 19.04 till the end of the experiment.

The wind direction increased from the beginning of the experiment to its peak at decimal date 18.92 then decreased until the end of the experiment. Two small and two large wind direction shifts were recorded during the 16th to the 20th of January 2006. The first two shifts in wind direction correlated well with the first two spikes in wind speed. The next two shifts in wind were more pronounced but did not correlate with increases in wind speed.

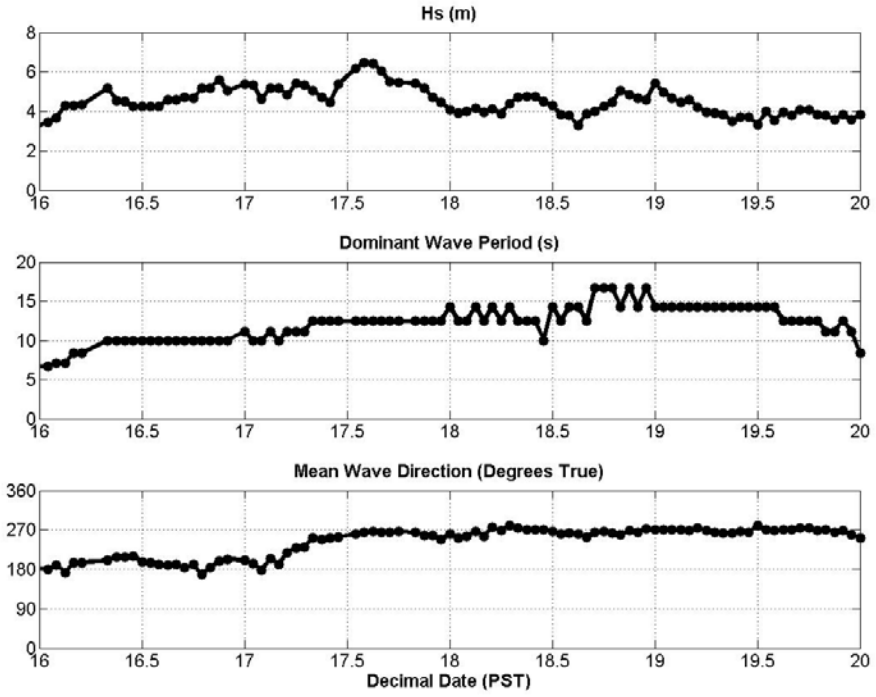

Figure 33 - Significant wave height (hs), wave period and direction for the MCR field deployment.

The significant wave height (Hs) increased from the beginning of the experiment to 6.47 meters at decimal date 17.58. From the peak of 6.47 meters at decimal date 17.58, the significant wave height decreased to 4 meters at decimal date 18.00. Two small spikes in significant wave height were recorded before the end of the experiment. They occurred at decimal date 18.38 and decimal date 19.00. The dominant wave period steadily increased from the beginning of the experiment to a peak of 16.7 seconds at decimal date 18.71. After which the wave period decreased until the end of the experiment. The waves were propagating from the south during the beginning of the experiment and shifted to the west at decimal date 17.54. The wave direction stayed from the west for the remainder of the experiment.

3.2 Data collection parameters

The same settings used during the FRF experiment for the Sitex radar were used in the MCR experiment. However, two different sets of digital collection parameters were used for the MCR experiment that varied from the digital collection parameters used for the FRF experiment. The first set was used from the 16th of January at 1805 to 17th of January at 0905 and the second set was used from 17th of January at 1005 to the 19th of January at 1805. The two collection parameters varied in the number of samples, the number of collections (i.e. degrees covered) and the offset. Table 11 shows the first set of digital collections parameters used for the MCR. Table 12 shows the second set of digital collection parameters used for the MCR.

Digital Collection Parameter Set #1 (16.75 to 17.38)	
Property	**Value**
Digital sampling rate	50 mhz
# of Rotations	640
# of waveforms to sum	4
# of samples per trigger	2048
# of collections per rotation	320
Acquisition Gate Delay	0
Offset	-320 db
Range Cell Size	3 meters
Maximum Range	6144 meters
Azimuth Cell Size	1.06 degrees
Degrees Covered	169 degrees

Table 11 - Digital collection parameter set #1 for MCR field deployment.

The offset is used to decrease the strength of the returned signal so that the data is not saturated, which can happen during periods of increased backscatter. The disadvantage of the offset is that it creates a minimum threshold for backscatter. Thus, no backscatter will be recorded if the backscatter from an illuminated cell is below the threshold. This presents unique data analysis challenges that must be accounted for. For example, the variance of a time series for a pixel could be 0 if the backscatter signal was not strong enough to overcome the offset threshold.

Digital Collection Parameter Set #2 (17.42 to 19.75)	
Property	**Value**
Digital sampling rate	50 mhz
# of Rotations	640
# of waveforms to sum	4
# of samples per trigger	2048
# of collections per rotation	485
Acquisition Gate Delay	0
Offset	-160 db
Range Cell Size	3 meters
Maximum Range	6144 meters
Azimuth Cell Size	1.06 degrees
Degrees Covered	257 degrees

Table 12 - Digital collection parameter set#2 for MCR field deployment.

Two data files were saved for every data collection as described previously for the FRF experiment. The nomenclature used for organizing data collections was slightly different for the MCR experiment. The first three digits of the data files are the date of the month in three digit format, the fourth and fifth digits are the hour and the sixth and seventh are the minute. All data collections were saved in Pacific Standard Time (PST) using a 24 hour time format. Just as before, the azimuth files were saved with an A preceding the day-time stamp and the raw data files were saved with an M preceding the day-time stamp. Therefore, the raw data file relating sample intensity to range and azimuth for the collection at 1905 on the 16th of January is M0161905.bin.

Analysis of the image stability for the MCR experiment was carried out in range-theta space. Initial visual observations of the range-theta images for the MCR experiment showed that the images were not stable. Figure 34 shows how the south jetty “drifts” throughout the rotations. Further, the collections for the next rotation are recorded at the end of the current rotation.

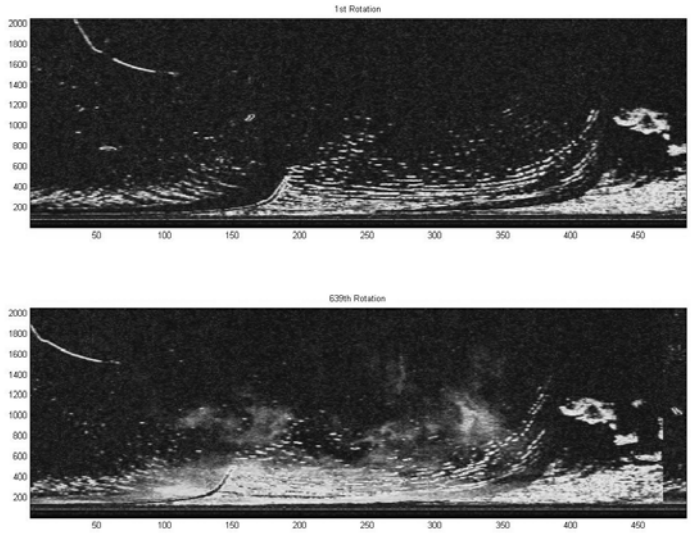

Figure 34 - Image shift of the MCR data. The top plot is the 1st radar rotation and the bottom plot is the last radar rotation. Notice how the image has shifted to the left.

The drift of the south jetty is also shown in Figure 35, which displays the plot of the pixel intensities for the furthest samples for each rotation.

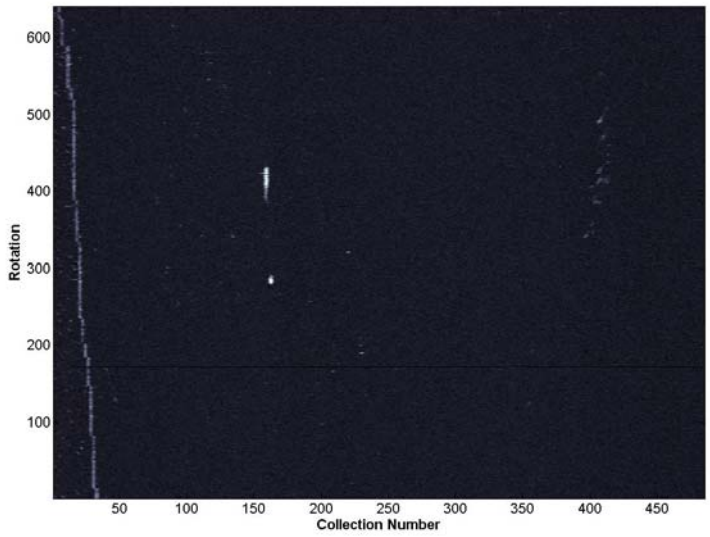

Figure 35 - South jetty drift. The furthest range for each rotation during one collection are plotted on top of each other. The bright white line to the left is the Trigger number in which the south jetty crosses into the picture.

The pixel at which the maximum intensity occurs along the furthest sample represents where the south jetty crosses into the radar image. The drift of the south jetty is obvious when all 640 rotations are stacked on each other.

The shift in the image is believed to be caused by the incorrect receiving/dropping of triggers by the data acquisition system. This problem was assumed to be caused by the variability in rpm. Image shifts of up to 70 pixels were observed in the data collections. The general drift of the radar implies that the radar rpm was faster than the calculated trigger recording time. A MATLAB script created by Pato Catalan was used to correct the data collections. Data collections after 0171005 were corrected and analyzed.

3.3 Results

Peak Period

Estimation of peak period for the MCR field deployment was carried out using the same process described for the FRF field experiment. However, raw data images were used for analysis instead of Cartesian images. The mean radar rpm for the MCR field experiment was 44.7 with a standard deviation of 2.2 rpm. The minimum RPM recorded was 37.8 and the maximum RPM recorded was 47.3. A RPM of 44.7 equates to a Nyquist frequency of 0.37 Hz. The frequency resolution remains the same as the FRF field deployment. Figure 36 is a plot of the raw data image.

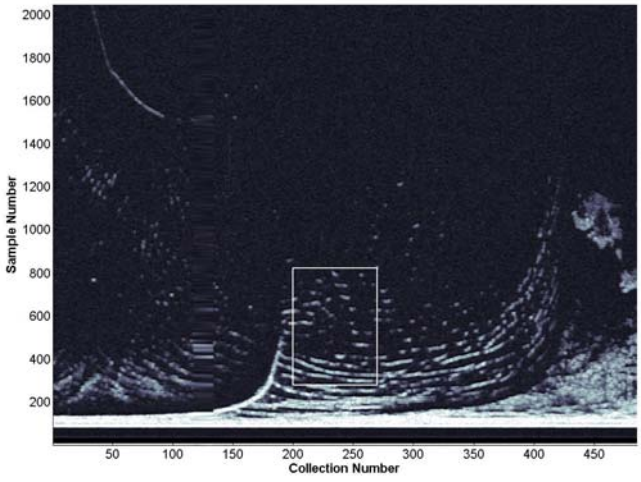

Figure 36 - The data window used to obtain peak period is overlaid on the raw data image for one revolution.

The image is presented with distorted axis to allow features along the x axis to be visible. These features would be difficult to see using an undistorted image since the number of samples is significantly larger than the number of triggers (creating a very tall and narrow image). The data window used for estimation of peak period is plotted as the white rectangle on Figure 36.

3D datacubes of pixel intensity time series were created from every fifth sample and trigger pixel inside the given data window by reading the binary data into MATLAB. Table 13 lists the minimum and maximum pixel coordinates for the period data window.

MCR period data window	Pixel Coordinates
Sample Number (min)	280
Sample Number (max)	825
Trigger Number (min)	200
Trigger Number (max)	270

Table 13 - Pixel coordinates of data window used to obtain peak period for MCR field deployment.

Figure 37 is the estimated dominant period obtained from the radar for the MCR field deployment compared to the dominant period from NOAA Buoy 46029.

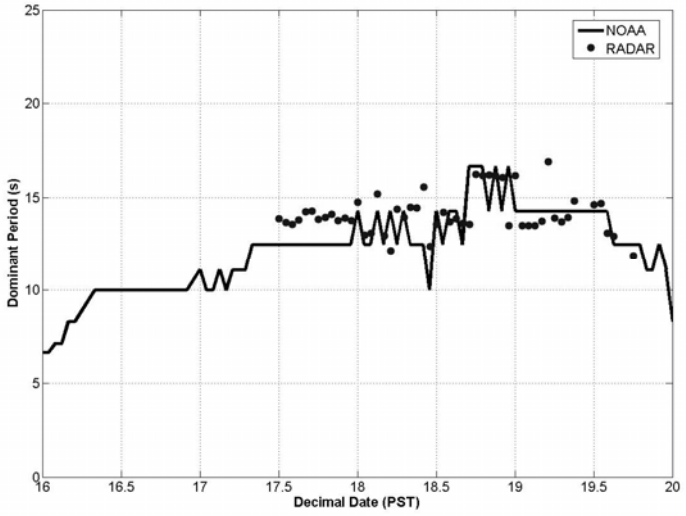

Figure 37 - Estimated period obtained from the radar compared to the in situ dominant period

The estimated wave periods from the radar agree well with the wave periods observed by the NOAA buoy. Figure 38 shows the image energy for the MCR field deployment. No clear correlations between environmental conditions and image energy could be drawn for the MCR field deployment.

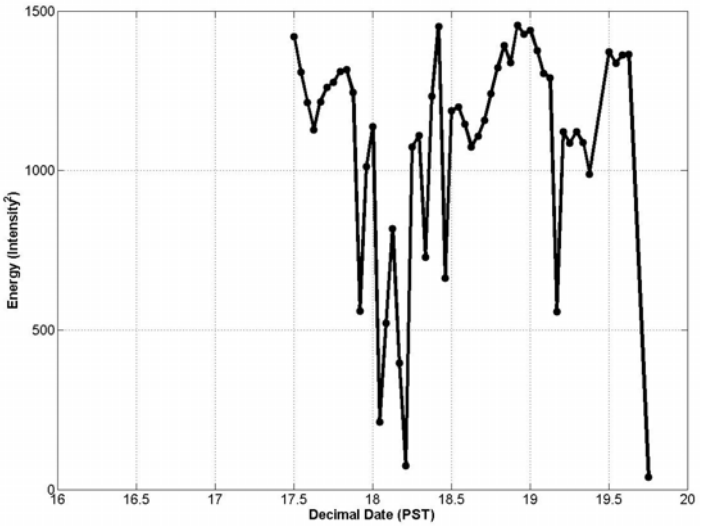

4. Discussion and Conclusion

A qualitative analysis of estimated radar periods and direction compared to in situ periods and direction showed good agreement for both field deployments. However, there were periods where the radar failed to accurately predict the ocean wave properties. These periods were most evident in the FRF field deployment. For the FRF deployment, the radar remote sensing system did not accurately predict wave periods during intervals of high frequency wind driven gravity waves. Additionally, during intervals of light wind conditions the wave periods returned from the radar showed an increase in variability. Further, the PSDs generated from the radar data during intervals of light winds showed less significant dominant peaks. The FRF field deployment also showed that wave direction obtained from the radar is more accurate during periods of strong radar backscatter. Wind speed was identified as the factor that most affected the radar estimation of the waves in the FRF field experiment. No clear correlations between environmental conditions and image energy could be drawn from the MCR field deployment.

Geo-locating the radar data for the FRF field deployment was difficult for two reasons. Having the GCPs in a straight line did not provide the ideal conditions for geo-locating the radar data and higher quality survey methods need to be used to locate the position of the GCPs. Ideally, the GCPs should be located to allow easy vertical and horizontal transformation of the coordinates. Also, the accuracy of the surveyed GCPs should be equal to or better than the accuracy of the remote sensing system.

Data analysis could benefit from the development of an image transfer function, which would connect the image properties to the wave properties. An image transfer function would also allow the PSDs to be directly integrated to obtain ocean wave properties. For this project, the effect of the high frequency variability on the dominant period was ignored. Integrating the spectrum to obtain the peak frequency using techniques that use the entire spectrum could improve the estimating capabilities of the radar.

Using a radar that has the capability of transmitting electromagnetic energy with shorter pulse lengths would decrease the Nyquist wavenumber of the system. This may not be completely necessary as seen from the analysis of Nyquist frequency and wavenumber presented earlier. However, it would be desirable to match spatial capabilities to the temporal capabilities of the radar system.

Future deployments will be immediately improved by conducting experiments in locations with a multitude of Ground control points. Coastal sites such as the MCR provide plenty of identifiable ground control points that can be used to geo-locate the image. Features such as bends in jetties, tips of piers and points of land provide sources of natural ground control points.

Future deployments could also be improved by locating an in situ sensor inside the area analyzed by the radar. Therefore, more direct comparisons between the two can be made. Additionally, collocating the in situ sensor within the illuminated area of the radar would allow the radar to be calibrated. This would enable the radar to estimate of wave significant height from the signal to noise ratio.

The proof of concept for NANOOS has demonstrated that the autonomous X-band radar remote sensing system being developed at Oregon State University is able to obtain ocean wave properties for MCR. The wave conditions of the Pacific Northwest are ideal for using radar remote sensing. Presently, a mobile trailer is being customized to house the data acquisition system, generator and radar. The trailer will have a 30 foot crank up tower that will be used as a stable platform for the antenna. Further, the trailer will have panels and possibly wind turbines to charge banks of batteries to allow for longer autonomous operation and time on scene.

5. References

Atanassov, V., Rosenthal W. and Ziemer F. Removal of ambiguity of two-dimensional power spectra obtained by processing ship radar images of ocean waves. Journal of Geophysical Research, 90 (C1), pp 1061-1067.

Dankert, H. and Rosenthal, W. (2004). Ocean surface determination from X-Band radar-image sequences. Journal of Geophysical Research, 109, pp C04016.

Defense Mapping Agency (1994). Radar navigation manual, NVPUB1310. 6th edition.

Heathershaw, A.D., Blackley M.W.L., and Hardcastle, P.J. (1980). Wave direction estimates in coastal waters using radar. Coastal Engineering, 3, pp. 249-267.

Izquierdo, P.; Guedes Soares, C.; Nieto Borge, J.C. and Rodriguez, G.R. (2004). A comparison of sea-state parameters from nautical radar images and buoy data. Ocean Engineering, 31 ,pp. 2209-2255.

Izquierdo, P.; Nieto Borge, J.; Guedes Soares, C.; González, R.S. & Rodríguez, G. (2005). Comparison of wave spectra from nautical radar images and scalar buoy data. Journal of Waterway, Port, Coastal, and Ocean Engineering. ASCE, 131 (3) ,pp. 123-131.

Izquierdo, P. and Guedes Soares, C. (2005). Analysis of sea waves and wind from X-band radar. Ocean Engineering, 32, pp. 1404-1419.

Lee, P.H.; Barter, J.D.; Beach, K.L.; Hindman, C.L.; Lake, B.M.; Rungaldier, H.; Shelton, J.C.; Williams, A.B. and Yuan, H.C. (1995). X band microwave backscattering from ocean waves , Journal of Geophysical Research, 100 (C2) ,pp. 2591-2611.

Mattie, M.G., Lee Haris, D. (1979). The use of imaging radar in studying ocean waves. Proceedings of the Coastal Engineering Conference, 1, pp. 174-189.

Nieto Borge, J.C. and Guedes Soares, C. (2000). Analysis of directional wave fields using X-band navigation radar. Coastal Engineering, 40 ,pp. 375-391.

Nieto Borge, J.C.; Reichert, K. and Dittmer, J. (1999). Use of nautical radar as wave monitoring instrument. Coastal Engineering, 37, pp. 331-342.

Raemer, H. R. (1997). Radar systems principles. CRC Press, Inc.

Robinson, I.S., Ward, N.P., Gommenginer, C.P, and Tenorio-Gonzales M.A (2000). Coastal oceanography applications of digital image data from marine radar. Journal of Atmospheric and Oceanic Technology, 17, pp. 721-725.

Seemann, J.; Ziemer, F. and Senet, C. (1997). A method for computing calibrated ocean wave spectra from measurements with a nautical X-band radar. Oceans' 97, 2 , pp. 1148-1154.

Trizna, D.B. (1991). Statistics of low grazing angle radar sea scatter for moderate and fully developed ocean waves. IEEE Transactions on Antennas and Propagation, 39 (12) ,pp. 1681-1690.

Trizna, D.B. (1997). A model for Brewster angle damping and multipath effects on the microwave radar sea echo at low grazing angles. IEEE Transactions on Geoscience and Remote Sensing, 35 (5), pp. 1232-1345.

Wolf, J. and Bell, P.S. (2001). Waves at Holderness from X-band radar. Coastal Engineering, 43, pp. 247-263.

Young, I.R.; Rosenthal, W. and Ziemer, F. (1985). A three-dimensional analysis of marine radar images for the determination of ocean wave directionality and surface currents. Journal of Geophysical Research, 90 (C1), pp. 1049-1059